Linear interaction of a cylindrical entropy spot with a shock

David Fabre[a] and Laurent Jacquin
ONERA, 29, av. de la Division Leclerc, BP 72, F-92322 Châtillon, France

Jörn Sesterhenn
Fachgebiet Strömungsmechanik, Technische Universität München, Boltzmannstr. 15, 85747 Garching, Germany

(Received 16 March 2001; accepted 15 May 2001)

The interaction of a cylindrical element of hot or cold gas (the ''entropy spot'') with a shock wave is considered. An exact solution in the limit of weak spot amplitudes is elaborated, using the linear interaction analysis theory and the procedure of decomposition proposed by Ribner (Technical Report No. 1164, NACA, 1953). The method is applied to an entropy spot with a Gaussian profile. Results are presented for a wide range of shock Mach numbers, with a special interest at $M_1=2$. The resulting vorticity field consists of a pair of primary counter-rotating vortices, as well as a pair of secondary vortices of opposite sign and weaker amplitude. An expression for the circulation in half a plane is derived and compared to existing results. The pressure field consists of a cylindrical acoustic wave which propagates away from the transmitted spot and an evanescent nonpropagative field confined behind the shock. For a hot spot, the cylindrical wave is a rarefaction wave on its forward front and a compression wave on its upstream propagating parts, and the nonpropagative field corresponds to a pressure deficit. The structure of the transmitted spot and the shock deformation are also discussed. The linear solution is compared with numerical simulation results for $M_1=2$ and $M_1=4$. The comparison shows qualitative and quantitative agreement when linear as well as nonlinear spot amplitudes are considered. Finally, the method is applied to the case of a constant spot with a tophat profile, and the results are compared to the case of a Gaussian spot. This paper also contains in the Appendix a general formulation of the linear interaction problem for the three kinds of plane waves (entropy, vorticity, and pressure waves) impinging upon a shock. [DOI: 10.1063/1.1383592]

I. INTRODUCTION

It is well known that the interaction of any of the three modes of fluctuation identified by Kovasznay[1] (the vorticity mode, the entropy mode, and the pressure mode) with a shock wave gives rise to the three modes downstream of the shock and to a perturbation of the shock surface. A theoretical basis of the problem has been given by the linear interaction analysis (LIA) theory initiated by the pioneering studies of Ribner[2] and Moore[3] and followed by other authors.[4–7] This theory describes the interaction of a plane wave of any of the three modes with a shock and allows calculation of the amplitudes of the three generated and transmitted waves. Since plane waves can be seen as the Fourier components of any flow field, the theory can, in principle, be applied to the interaction of an arbitrary weakly perturbed flow field with a shock.

The approach has been applied by Ribner[8] to homogeneous turbulence without entropy fluctuations. The turbulence amplification rates and acoustic generation levels predicted by the theory have been compared to direct numerical simulations,[9–11] and to rapid distortion theory.[12] Ribner also used the LIA method to characterize the cylindrical sound wave formed by the interaction of an isolated vortex with a shock wave.[13,14] In these references, the theoretical result has been successfully compared to a shock tube experiment.[15]

The role of the entropy mode in shock-turbulence interaction has been outlined in a series of analytical and computational studies by Mahesh *et al.*[16,17] These authors have shown that for strong shocks, the shock-turbulence interaction is strongly influenced by the entropy fluctuations. This motivates new interest in the case of flows involving entropy fluctuations.

Apart from its academic interest, the problem of shock-entropy interaction is relevant to aerospace applications. For example, in supersonic wakes and jets, the entropy variations are found to be very large and the interaction with oblique shocks is thought to be an important source of noise. On the other hand, the mechanism of shock-induced vorticity generation (described below) could be helpful to increase the efficiency of high speed combustion systems.[18,19]

The ''entropy spot'' considered in this paper constitutes one of the most simple forms of a localized entropy perturbation; it consists of a cylindrical element of fluid characterized by a higher (or lower) temperature than the surrounding fluid. The interaction of this ''entropy spot'' with a shock wave leads to a variety of physical phenomena that can be

[a]Telephone: (+33)1 46 23 51 64; fax: (+33)1 46 23 51 58; electronic mail: David.Fabre@onera.fr

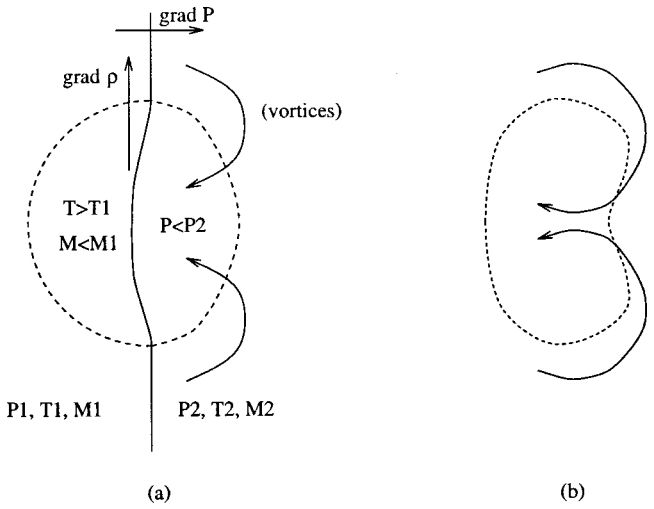

FIG. 1. Qualitative description of the interaction.

described as follows, for the case of a hot spot [Fig. 1(a)]:

(1) The initially circular spot is compressed and acquires an elliptic shape.
(2) In the center of the spot, the Mach number is lower than in the surrounding fluid. As a consequence, the pressure jump is weaker, and a low pressure region forms behind the shock. This low pressure region leads to a deformation of the shock surface.
(3) Additionally, this low pressure region propagates away and forms a cylindrical sound wave.
(4) Finally, the combination of the density gradient and the pressure gradient leads to a baroclinic torque, which creates a symmetrical vorticity structure.

Thus the flow field can be thought of as an elliptic spot, a pair of counter-rotating vortices, and a cylindrical rarefaction wave. The same phenomenology applies to the case of a cold spot, if the phenomena are considered with the opposite sign.

The later evolution of the spot is sketched in Fig. 1(b). Under the influence of its own velocity, the transmitted spot rolls up and the high temperature regions concentrate into the vortical regions. In addition, if it is strong enough, the sound wave may steepen or flatten depending on its compression or rarefaction nature.

The main features of the interaction described above have been observed in a variety of shock-tube experiments, such as a shock wave interacting with a column of heated fluid resulting from a wire explosion,[20,21] spherical flames,[22,23] cylindrical and spherical bubbles of lighter and heavier gas,[22,24] and a cylindrical jet of light gas.[25] Note that some of these experiments involve additional effects such as differences in the gas properties, interface effects, chemical reactions, or three-dimensional effects. However, all the experiments seem to be basically governed by the shock-entropy interaction mechanism presented above.

The problem has also received an important computational effort,[26–31] and the general features of the interaction which have been observed are in qualitative accordance with the experiments. However, differences can be observed between the computations which used a smooth entropy distribution as an initial condition (e.g., a Gaussian spot[30]), and those which used a sharp one (e.g., a constant spot[27]).

A number of analytic developments for the problem have been undertaken. Haas and Sturtevant[24] developed a model based on geometrical acoustics to determine the geometry of the pressure waves. The method can only provide qualitative results, but which are in accordance with experiments. It can apply to a strong entropy amplitude in the spot, but it is limited to weak shock waves. Very recently, Grasso and Pirozzoli[31] have formulated an acoustic analogy of the problem that leads to an expression for the pressure field in the acoustic wave. Their model applies for either weak shocks or weak spot amplitudes. Efforts have also been made to determine the circulation of the vortex pair, and several models have been elaborated, in particular by Rudinger and Somers,[22] Picone *et al.*,[26,27] and Yang *et al.*[29] However, a complete analytical solution of the problem, describing the vorticity and pressure generation as well as the shock deformation and the compression of the spot, is still missing.

The goal of this paper is to provide a complete solution of this interaction using the LIA method and the procedure of decomposition used by Ribner for the shock-vortex interaction.[13,14] The paper is organized as follows: In Sec. II the procedure of decomposition is described qualitatively; then in Sec. III it is applied to the case of a Gaussian entropy spot. In Sec. IV detailed results are given for a Mach 2 shock, and the characteristic features of the solution are presented for a wide range of Mach numbers. In Sec. V the linear solution is compared with numerical simulation results. Finally, the application of the method to the case of a constant spot is presented in Sec. VI and the differences with the Gaussian spot are discussed.

II. QUALITATIVE DESCRIPTION OF THE PROCEDURE

In this section the procedure used to treat the interaction is described qualitatively.

As stated in the Introduction, the interaction of a plane entropy wave with a shock gives rise to a triad of waves behind the shock (a detailed solution to this problem is given in Appendix A). Depending upon the angle of incidence of the impinging wave, two different regimes may be obtained. In the propagative regime (see Fig. 2), the pressure wave propagates away as an acoustic wave, and the three generated waves are in phase with the incident wave. In the nonpropagative regime (Fig. 3), the amplitude of the pressure wave decays exponentially away from the shock, and there is a phase shift between the generated waves and the incident wave.

Using one-dimensional Fourier synthesis, plane entropy waves in the same direction can be arranged together to represent parallel entropy distributions. Such a parallel entropy distribution, referred hereafter as an ''entropy slice,'' is represented in Fig. 4(a). Positioning elementary entropy slices radially in all the angular directions, just as the spokes of a wheel, one can construct a cylindrical entropy distribution, i.e., an entropy spot. This construction procedure of an iso-

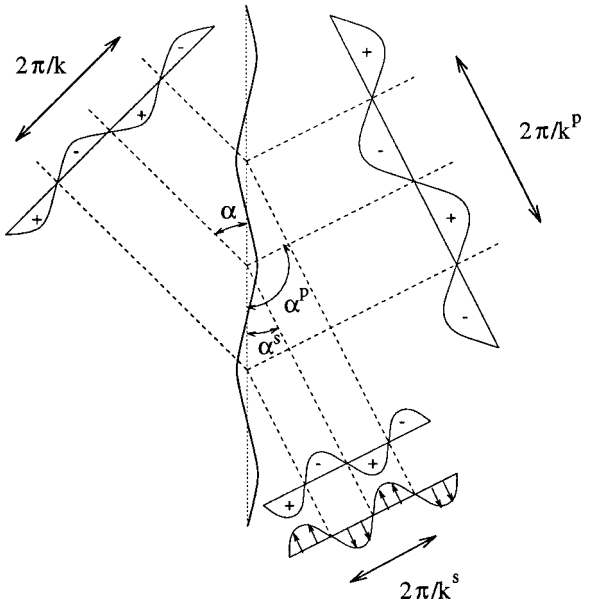

FIG. 2. Interaction of an entropy wave with a shock wave (propagative regime).

lated entropy spot as a sum of elementary entropy slices is sketched in Fig. 4. It is identical to the procedure used by Ribner to construct an isolated vortex as a sum of elementary shear flows.[13,14]

When the spot is convected through a shock, the interaction of the elementary slices with the shock follows the same rules as the constituent elementary waves. For each elementary slice, the interaction leads to a transmitted entropy slice, a generated vorticity slice, as well as a pressure perturbation and a shock deformation. This is represented in Fig. 5 for two particular slices, which have been chosen such that the interaction of the first slice (angle α) is of the propagative type, and the interaction of the second slice (angle α')

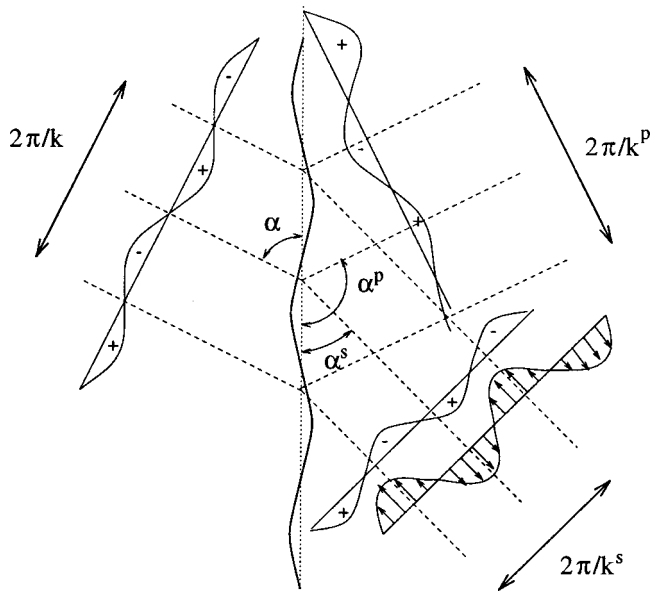

FIG. 3. Interaction of an entropy wave with a shock wave (nonpropagative regime).

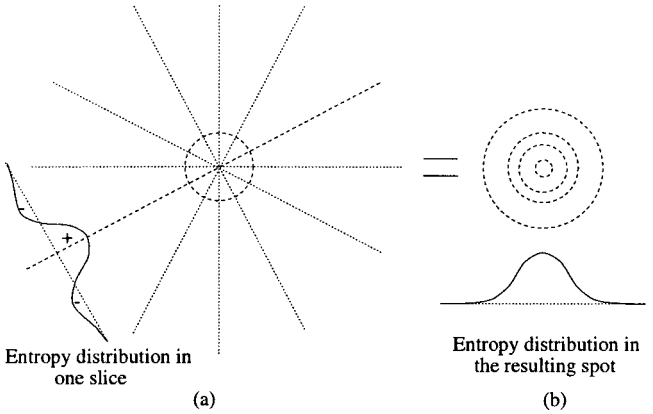

FIG. 4. Illustration of the "slice decomposition" of the spot.

is of the nonpropagative type. The generated entropy slices (not represented in Fig. 5) will then focus on the center of the transmitted spot. The resulting entropy spot can thus be obtained by rearranging the different transmitted entropy slices.

Similarly, the combination of the generated vorticity slices results in the vortical structures. Note that the elementary vorticity slice generated for initial angle α' in Fig. 5 has an asymmetric profile. This is due to the phase shift on the constituent plane waves.

The interaction of the slice with angle α gives rise to an generated pressure slice with the same profile. This elementary pressure perturbation propagates away at the speed of sound C_2. At a time t after the instant when the center of the spot has crossed the shock, the elementary pressure profiles corresponding to angles α in the propagative range will all be tangent to a circle of radius $R=C_2t$ centered on the transmitted spot. All these elementary slices will therefore contribute to a cylindrical sound wave. This construction is illustrated in Fig. 6.

The pressure perturbation resulting from the interaction of the second slice with angle α' in Fig. 5 has a different

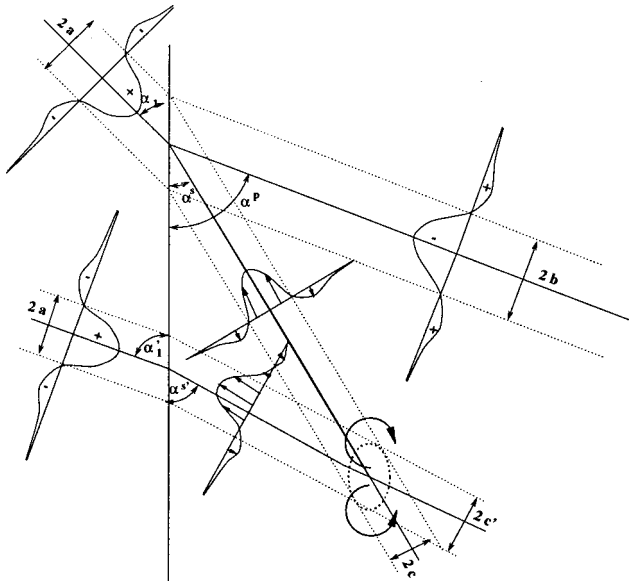

FIG. 5. Interaction of two particular elementary slices with the shock.

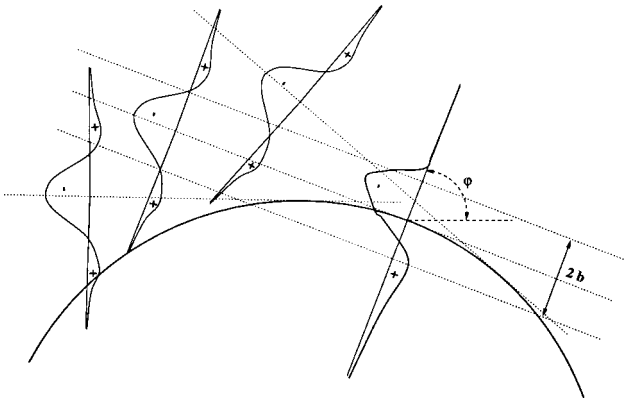

FIG. 6. Illustration of the formation of the cylindrical acoustic wave.

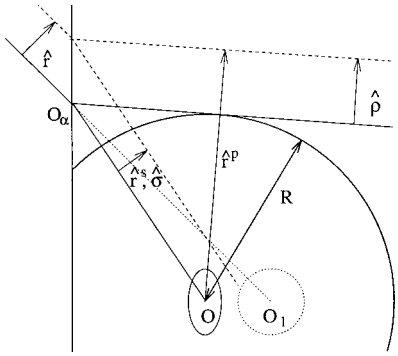

FIG. 7. Details about the geometrical procedure. Illustration of the change of origin from the virtual center O_1 of the incident spot, to the point O_α on the shock front, and then to the center O of the transmitted spot.

behavior. All the constituent elementary pressure waves decay away from the shock independently from each other, so the corresponding pressure field does not maintain an identifiable shape. Therefore, it has not been represented in Fig. 5.

III. DETAILED ANALYSIS FOR A GAUSSIAN SPOT

The initial flow field we will consider hereafter consists of an entropy spot with a Gaussian profile of radius a and amplitude ϵ centered on the point O_1, carried by a mean flow of temperature T_1, density ρ_1 and velocity U_1, i.e.,

$$\frac{s'}{C_p}=\epsilon e^{-(r^2/a^2)}, \tag{1}$$

where r is the radial coordinate relative to O_1, and where the entropy fluctuation is made nondimensional with the specific heat C_p of the gas (the ratio of specific heats is $\gamma=C_p/C_v=1.4$). In the limit of small amplitude ϵ, the corresponding temperature and density fields are given by $\theta=T_1(1+(s'/C_p))$ and $\rho=\rho_1(1-(s'/C_p))$.

In order to describe this spot as a superposition of plane entropy waves, we perform a two-dimensional Fourier transform of Eq. (1). Using polar coordinates (r,ϕ) in the physical plane and (k,α) in the spectral plane, this results in

$$\frac{s_1'}{C_p}=\frac{\epsilon}{2\pi}\int_0^\pi\int_0^\infty e^{-[(ka)^2/4]}e^{ikr\cos(\alpha-\phi)}ka\,d(ka)\,d\alpha, \tag{2}$$

where the real part must be retained.

Reassembling the contributions of all wave numbers of the same angle α gives

$$\frac{s_1'}{C_p}=\frac{\epsilon}{\pi}\int_0^\pi K\left(\frac{\hat r}{a}\right)d\alpha, \tag{3}$$

where $\hat r=r\cos(\alpha-\phi)$ is the variable describing planes of constant phase in the angular direction α, and where

$$K(z)=\int_0^\infty\frac{k}{2}e^{-(k^2/4)}\cos(kz)dk=1-2z\mathcal{F}(z). \tag{4}$$

Function $\mathcal{F}(z)$ is the Dawson integral (see Ref. 32, p. 298) defined as

$$\mathcal{F}(z)=e^{-z^2}\int_0^z e^{t^2}dt. \tag{5}$$

Equation (3) is the mathematical expression of the "slice decomposition" introduced in Sec. II and described in Fig. 4. The function K is the equivalent of the function g in Ribner's analysis of an isolated vortex [Eq. (8) of Ref. 14].

At a time t after the instant when the center of the spot has crossed the shock, the virtual center O_1 of the initial spot has been convected a distance of U_1t from the shock, and each elementary slice crosses the shock at a point O_α corresponding to coordinates $(-U_1t,U_1t\cot\alpha)$ in the frame centered on O_1 (see Fig. 7). The interaction of each elementary entropy wave $e^{ik\hat r}$ appearing in expression (2) gives rise to an entropy wave $Z_{ss}e^{ik^s\hat\sigma}$, a vorticity wave $Z_{sv}e^{ik^s\hat\sigma}$, and a pressure wave $Z_{sv}e^{ik^p\hat\rho}e^{-k^p\eta\overline{x}}$. Here $\hat\sigma$ and $\hat\rho$ are the variables describing planes of constant phase in the directions α^s and α^p (the origin is situated at the point O_α), and $\overline{x}$ is the distance from the shock front. The relative amplitudes Z_{ss}, Z_{sv}, Z_{sp}, Z_{sx}, and the geometrical characteristics k^s, α^s, k^p, α^p, η of these waves are given in Appendix A.

Making use of the geometrical relation $\cot\alpha^s=m\cot\alpha$ with $m=U_1/U_2$ [Eq. (A8) of Appendix A], it can be seen that all the entropy and vorticity waves generated downstream of the shock focus on the point O with coordinates $((U_2-U_1)t,0)$ in the frame centered on O_1. Point O corresponds to the center of the transmitted spot (see Fig. 7). Using a frame of reference centered on point O leads to a simplification of the different components of the flow field. The coordinates of point O_α in that frame are

$$x_c=-U_2t,\quad y_\alpha=U_2t\cot\alpha^s.$$

We introduce the variables $\hat r^s=r\cos(\alpha^s-\phi)$ and $\hat r^p=r\cos(\alpha^p-\phi)$, where (r,ϕ) are now polar coordinates centered on O. Using Eqs. (A8) and (A12) one may then verify that the change of origin from O_α to O amounts to

$$\hat r^s=\hat\sigma, \tag{6}$$

$$\hat r^p=\hat\rho+R, \tag{7}$$

where $R=C_2t$ is the radius of the cylindrical sound wave at the instant considered (the second relation is only valid in the propagative regime). All these geometrical details are repro-

duced in Fig. 7. Note that similar geometrical manipulations were used by Ribner[13,14] to study the shock/vortex interaction.

The expressions for the entropy and vorticity fields can then be simplified further by introducing the length c such that for each plane wave, $k^s c = ka$, and the Jacobian $J^s = \partial\alpha/\partial\alpha^s$. Similarly, in order to simplify the evaluation of the pressure field in the propagative regime, we will introduce the length b such that $k^p b = ka$, and the Jacobian $J^p = \partial\alpha/\partial\alpha^p$. Note that the length c can be interpreted as the radius of the transmitted spot, when observed under the angle α^s. This is illustrated in Fig. 5. Similarly, the length b corresponds to the width of the elementary pressure slice at angular location α^p. The expressions for $c/a = k/k^s$, $b/a = k/k^p$, J^s, and J^p are given in Appendix A.

Using all these expressions, the entropy, solenoidal velocity and vorticity fields take a concise form, similar to Eq. (3),

$$\frac{s'}{C_p} = \frac{\epsilon}{\pi}\int_0^{\pi}\left[\Re(Z_{ss})K\left(\frac{\hat{r}^s}{c}\right) - \Im(Z_{ss})L\left(\frac{\hat{r}^s}{c}\right)\right]J^s d\alpha^s, \tag{8}$$

$$\frac{u'}{U_2} = \frac{\epsilon}{\pi}\int_0^{\pi}\left[\Re(Z_{sv})K\left(\frac{\hat{r}^s}{c}\right) - \Im(Z_{sv})L\left(\frac{\hat{r}^s}{c}\right)\right]\sin\alpha^s J^s d\alpha^s, \tag{9}$$

$$\frac{v'}{U_2} = -\frac{\epsilon}{\pi}\int_0^{\pi}\left[\Re(Z_{sv})K\left(\frac{\hat{r}^s}{c}\right) - \Im(Z_{sv})L\left(\frac{\hat{r}^s}{c}\right)\right]\cos\alpha^s J^s d\alpha^s, \tag{10}$$

$$\frac{\omega' a}{U_2} = -\frac{\epsilon}{\pi}\int_0^{\pi}\left[\Re(Z_{sv})K'\left(\frac{\hat{r}^s}{c}\right) - \Im(Z_{sv})L'\left(\frac{\hat{r}^s}{c}\right)\right]\times\left(\frac{a}{c}\right)J^s d\alpha^s. \tag{11}$$

In these expressions, $\Re$ and $\Im$ denote the real and imaginary parts of the complex transfer functions, and $L(z)$ is a new profile function, defined as

$$L(z) = \int_0^{\infty}\frac{k}{2}e^{-(k^2/4)}\sin(kz)dk = \sqrt{\pi}ze^{-z^2}. \tag{12}$$

K' and L' are the derivatives of functions K and L, with functional form,

$$K'(z) = -2z - (2-4z^2)\mathcal{F}(z),$$
$$L'(z) = \sqrt{\pi}(1-2z^2)e^{-z^2}. \tag{13}$$

Applying the same procedure to the pressure field gives

$$\frac{p'}{P_2} = \frac{\epsilon}{\pi}\int_{-\alpha_c^p}^{\alpha_c^p}K\left(\frac{\hat{r}^p - R}{b}\right)Z_{sp}J^p d\alpha^p + \frac{\epsilon}{2\pi}\int_{\alpha_c}^{\pi-\alpha_c}Z_{sp}d\alpha \times\int_0^{\infty}e^{-[(ka)^2/4]}e^{k^p[i\hat{\rho}-\eta(x-x_c)]}kad(ka), \tag{14}$$

where the two terms on the right-hand side account for the contribution of the propagative and nonpropagative plane waves, respectively. Since the plane pressure waves of the nonpropagative type decay exponentially independently from each other, the second term of this expression cannot be simplified further.

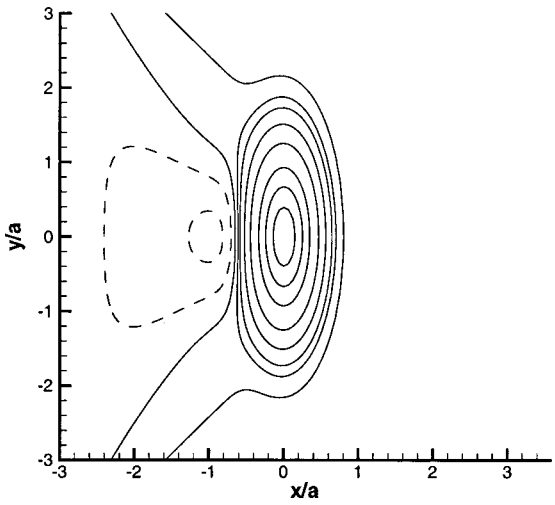

FIG. 8. Entropy field in the transmitted spot for $M_1 = 2$. Levels correspond to -0.03, -0.01, 0.01, 0.03, 0.05, 0.1, 0.2, 0.4, 0.6, and 0.8.

Finally the shock displacement takes the form,

$$\frac{X_c'}{a} = \frac{\epsilon}{\pi}\int_0^{\pi}\left[\Re(Z_{sx})K^I\left(\frac{(y-y_\alpha)\sin\alpha^s}{c}\right) - \Im(Z_{sx})L^I\left(\frac{(y-y_\alpha)\sin\alpha^s}{c}\right)\right]J^s d\alpha^s, \tag{15}$$

with functions K^I, L^I defined as

$$K^I(z) = \int_0^{\infty}\frac{1}{2}e^{-(k^2/4)}\cos(kz)dk = \frac{\sqrt{\pi}}{2}e^{-z^2}, \tag{16}$$

$$L^I(z) = \int_0^{\infty}\frac{1}{2}e^{-(k^2/4)}\sin(kz)dk = \mathcal{F}(z). \tag{17}$$

Note that in these expressions, the entropy and solenoidal velocity fields do not depend upon time and are convected like ''frozen patterns,'' whereas the pressure field and the shock deformation are explicitly time-dependent (through R and y_α). Note also that Eqs. (9) and (10) only correspond to the vortical part of the velocity field. The potential part of the velocity field, which is related to the pressure field, is not detailed here.

IV. RESULTS FOR A GAUSSIAN SPOT

A. Entropy field

The entropy field given by Eq. (8) is represented in Fig. 8 for $M_1 = 2$. As expected, after compression by the shock, the spot has acquired a roughly elliptic shape. One further notices the existence of a secondary spot of opposite sign in the wake of the main transmitted spot. Also, the entropy contours in the periphery of the main spot are distorted backward. It can be noted that the direction of this distortion corresponds to the separating angle α_c^s between the propagative and nonpropagative regimes: for $M_1 = 2$, this critical

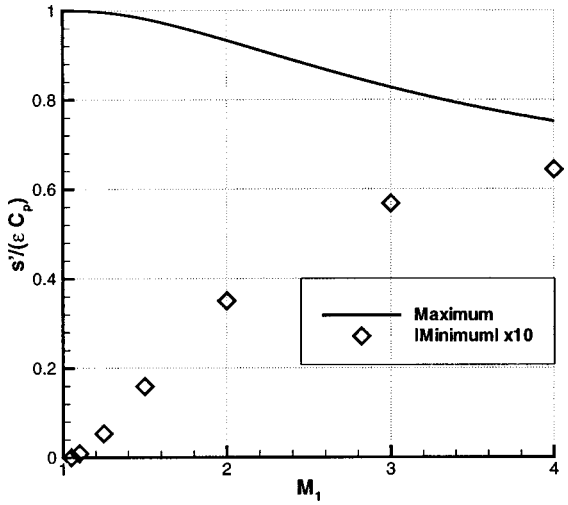

FIG. 9. Maximum entropy fluctuation in the transmitted spot, and minimum of entropy in the secondary spot (multiplied by 10) as functions of the shock Mach number.

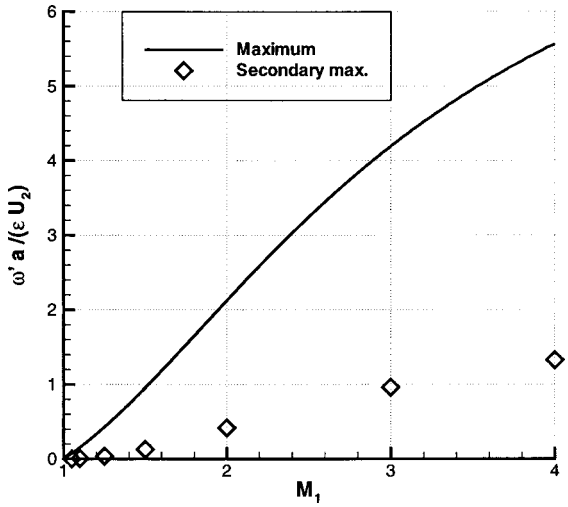

FIG. 11. Maximum vorticity in the primary and secondary vortices as functions of the shock Mach number.

angle is $\alpha_c^s \approx 35°$ [Eq. (A10) of Appendix A]. This effect can be attributed to the peak of the transfer function Z_{ss} at this critical angle.

The maximum value of the entropy fluctuation in the center of the transmitted spot is represented in Fig. 9, for M_1 varying continuously from 1 to 4. This maximum value is found to decrease as the shock strength increases. [It must be kept in mind that the base flow (the unperturbed shock) is not isentropic.] Absolute values of the minimum in the secondary spot have also been reported in Fig. 9 for a few values of M_1. The amplitude of this secondary spot grows with the Mach number, but remains at least 10 times lower than the amplitude of the main spot.

B. Vorticity field

The vorticity field given by Eq. (11) is shown in Fig. 10 for $M_1=2$. As expected, the flow field mainly consists of a pair of counter-rotating vortices. In addition, a secondary pair of weaker vortices of opposite sign is observed in the wake of the primary pair. As for the entropy field, the vortices are stretched in the direction of the critical angle α_c^s. This is also due to the peak in the transfer function at this particular angle.

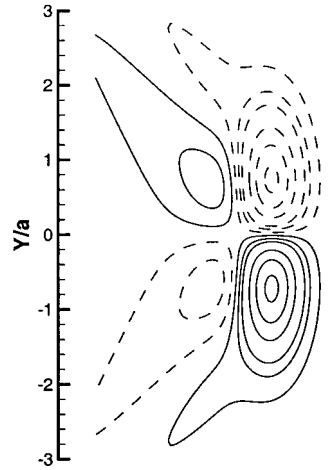

FIG. 10. Vorticity field from linear theory ($M_1=2$). Levels correspond to 0.1, 0.3, 0.5, 1, 1.5, 2 and the dashed line corresponds to negative values.

Figure 11 displays the maximum values of the vorticity in the primary vortices (for M_1 ranging continuously from 1 to 4) and in the secondary vortices (for a few values of M_1).

The expression of the velocity field given by Eqs. (9) and (10) can be manipulated to obtain an expression for the circulation in the upper (or lower) half plane. Calculations are reported in Appendix B. The nondimensional circulation takes the very simple form,

$$\frac{\Gamma}{aU_2}=\frac{2(m-1)}{m}f\epsilon, \tag{18}$$

where $m=U_1/U_2$ is the compression rate of the shock and $f=\sqrt{\pi}/2$ for a Gaussian spot. Note that this value corresponds to the circulation in half a plane, and contains the contribution of the primary and secondary vortices. The circulation of the primary vortices, considered alone, may be slightly higher.

We now compare this expression with previous expressions proposed in the literature. The most elaborate model is due to Picone *et al.*[26] These authors computed the vorticity by integrating the baroclinic production term during the interaction, and integrated it over a half plane in order to evaluate the circulation. The hypothesis was made that the shock remains straight during the interaction. Their result is

$$\Gamma_P=2V_2\left(1-\frac{V_2}{2U_1}\right)af\ln(\rho_1/\rho_0), \tag{19}$$

where ρ_0 is the value of the density at the center of the initial spot, $V_2=U_1-U_2$, and the factor f is also $\sqrt{\pi}/2$ for a Gaussian spot. Considering linear spot amplitudes ($\ln(\rho_1/\rho_0)=\epsilon$), and using our notation, Eq. (19) can be written

$$\frac{\Gamma_P}{aU_2}=\frac{m^2-1}{m}f\epsilon. \tag{20}$$

In the limit of weak shocks ($m \to 1$), Eqs. (18) and (20) are equivalent. For stronger shocks, Eq. (20) leads to an overprediction; for an $M_1 = 2$ shock, the ratio Γ_P/Γ is 1.83, and it can be as much as 3.5 in the limit of very strong shocks.

In a more recent paper, Yang *et al.*[29] checked all the existing models (including the one from Picone *et al.*) against numerical results. They noticed that all the models overpredicated the computed circulation for strong shocks. They proposed an expression based on dimensional analysis with correlation which fits most of their numerical results,

$$\Gamma_Y = \frac{4aC_1}{\gamma M_1}\frac{\rho_1}{\rho_2}\left(\frac{P_2}{P_1}-1\right)\left(\frac{1-\rho_0/\rho_1}{1+\rho_0/\rho_1}\right). \tag{21}$$

Considering again linear spot amplitudes, and writing the pressure jump and the Mach number M_1 as functions of the compression rate m leads to

$$\frac{\Gamma_Y}{aU_2} = \frac{2(m-1)}{m}\epsilon. \tag{22}$$

So for weak spot amplitudes, the expression from Yang *et al.*[29] is equivalent to ours except for the presence of the form factor f. However, Yang *et al.* did not consider a Gaussian profile, but a sharper one. It will be shown in Sec. VI that their result is retrieved when considering a constant entropy spot.

Finally we address the validity of the vorticity field predicted by the linear solution during the later stages of the interaction. If we exclude the possibility of three-dimensional instabilities, the evolution after the interaction is governed by the two-dimensional Navier–Stokes equation. For the u-component of the velocity,

$$\frac{\partial u}{\partial t} + u\frac{\partial u}{\partial x} + v\frac{\partial u}{\partial y} = -\frac{\partial p}{\partial x} + \nu\left(\frac{\partial^2 u}{\partial x^2} + \frac{\partial^2 u}{\partial y^2}\right). \tag{23}$$

Dimensional analysis shows that two time scales appear in this equation; a nonlinear time scale $T_{\rm nl} = a/|u'|$, where $|u'|$ is a characteristic value of the velocity field in the vortices, and a viscous time scale $T_v = a^2/\nu$. The velocity field predicted by the linear solution [Eqs. (9)–(11)] may be considered as valid for $t \ll T_{\rm nl}$ and $t \ll T_v$. Integrating both sides of Eq. (23) for x varying from $-\infty$ to $+\infty$, and supposing that the velocity field remains symmetric during the roll-up, leads to

$$\frac{d\Gamma}{dt} = \nu\int_{-\infty}^{+\infty}\frac{\partial^2 u}{\partial y^2}\,dx. \tag{24}$$

Equation (24) shows that the circulation in half a plane only evolves on the viscous time scale T_v. So the validity of the circulation predicted by Eq. (18) only requires $t \ll T_v$. These results show that if the Reynolds number $\mathrm{Re} = |u'|a/\nu \equiv T_v/T_{\rm nl}$ of the vortices is high, then the later evolution will consist of two stages: first, an inviscid roll-up with constant circulation on the time scale $T_{\rm nl}$, and then a slow viscous diffusion on the time scale T_v.

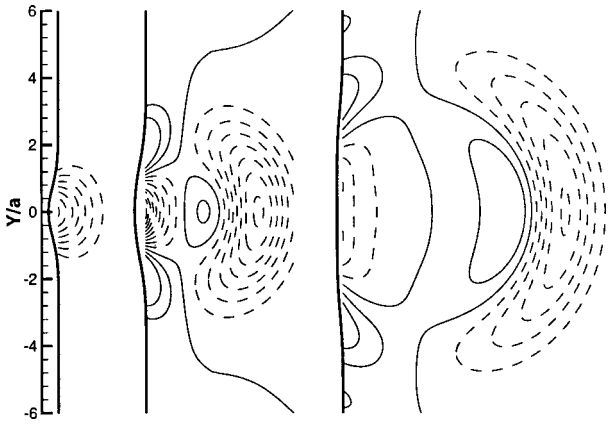

FIG. 12. Pressure field $p'/\epsilon P_2$ and shock deformation $X_c'/\epsilon a$ from linear theory ($M_1 = 2$), at three different instants corresponding to $R/a = 0$, 2, and 4. The step between two levels is 0.05 (for $R/a = 0$) and 0.02 (for $R/a = 2$ and 4).

C. Pressure field

The pressure field given by Eq. (14) is plotted in Fig. 12 for $M_1 = 2$ and for three different instants of the interaction corresponding to $R/a = 0$, $R/a = 2$, and $R/a = 4$. The first plot corresponds to the instant when the center of the spot crosses the unperturbed shock. As expected, the pressure field is then characterized by a low pressure region into the spot. Later, the low pressure region propagates downstream and forms a cylindrical rarefaction wave. In addition, we note that in the vicinity of the shock front, the generated pressure wave is a compression wave. Finally, we remark that a region of low pressure remains downstream of the shock. This ''near field'' corresponds to the contribution of nonpropagative pressure waves.

In the later stages of the interaction, the pressure field consists of a cylindrical acoustic wave except in the vicinity of the shock. An asymptotic expression for this cylindrical wave is developed in Appendix C for $R/a \gg 1$. The result is

$$\frac{p'}{P_2} \approx \frac{\epsilon}{\pi}\sqrt{\frac{2a}{R}}\,\mathbf{F}(\phi;M_1)\tilde{K}\left(\frac{r-R}{b_\phi}\right), \tag{25}$$

with functions $\mathbf{F}$ and $\tilde{K}$ defined as

$$\mathbf{F}(\phi;M_1) = \left(J^p Z_{sp}\sqrt{\frac{b}{a}}\right)_{\alpha^p=\phi}, \tag{26}$$

$$\tilde{K}(z) = \int_0^\infty \frac{1}{\sqrt{z'}}K(z-z')\,dz'. \tag{27}$$

Expression (25) has the same form as the one given by Ribner for the shock/vortex interaction [Eq. (23) of Ref. 13]. It consists of the product of the following terms:

(a) The first term $\sqrt{2a/R}$ describes the temporal evolution of the circular wave. Remember that the radius $R = C_2 t$ is a measure of time, so the temporal evolution is porportional to $t^{-1/2}$, as expected for a two-dimensional acoustic wave.

(b) The second term $\mathbf{F}(\phi;M_1)$ is the angular description of the wave. This function is represented for several val-

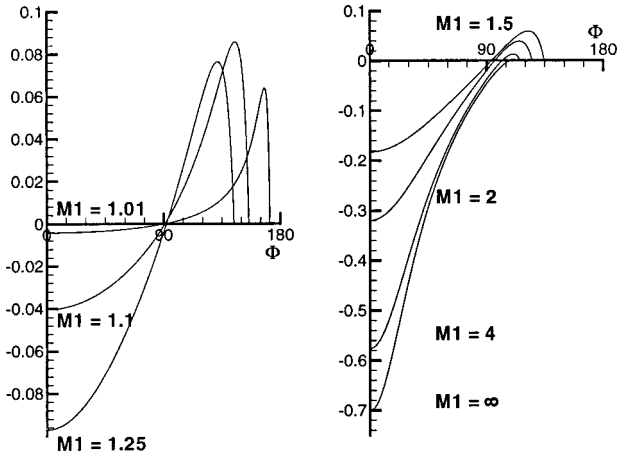

FIG. 13. Angular amplitude $\mathbf{F}(\phi;M_1)$ of the cylindrical pressure wave.

ues of M_1 in Fig. 13. It can be seen that for moderate Mach numbers, this function changes its sign around the angle $\phi=90°$. The acoustic wave therefore has an alternating structure. For a hot spot, it is a rarefaction wave on its downstream propagating part ($0<\phi<90°$), and a compression wave on its upstream propagating part ($90°<\phi<\alpha_c^p$). This formally corresponds to the emission of a dipolar acoustic source. For large Mach numbers, this alternating structure disappears, and the emission is similar to that resulting from a monopolar acoustic source.

(c) The last term $\tilde{K}((r-R)/b_\phi)$ is the radial description of the wave. This function is represented in Fig. 14. It possesses a maximum $\tilde{K}(0.41)=1.3666$, and a secondary minimum $\tilde{K}(-1.22)=-0.635$. So in its widest part, the sound wave resulting from a hot spot is a rarefaction wave followed by a recompression of lower amplitude.

The validity of the asymptotic expression (25) has been checked against the integral expression (14). The convergence is rapid. For $(R/a)=4$ and $M_1=2$, which is the third instant plotted in Fig. 12, the asymptotic value is already reached on the downstream front of the wave. This differs from the case of shock–vortex interaction.[14] In this later case, it was observed that the cylindrical sound wave was preceded by a ''precursor'' wave, resulting from the potential

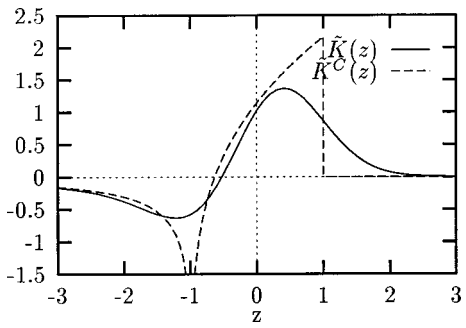

FIG. 14. Pressure profiles in the cylindrical acoustic wave: $\tilde{K}(z)$ for a Gaussian spot, and $\tilde{K}^C(z)$ for a constant spot (to be described in Sec. VI).

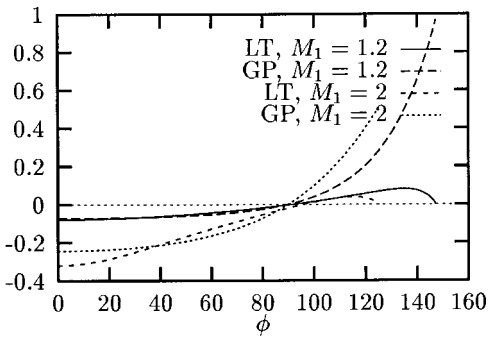

FIG. 15. Angular amplitude of the acoustic wave predicted by Grasso and Pirozzoli's acoustic analogy (GP) and by the linear theory (LT), for $M_1=1.2$ and $M_1=2$.

flow around the vortex core. The amplitude of this wave was found to decay as t^{-1} rather than $t^{-1/2}$. This is not observed in the case of an entropy spot. Finally, one must remind that the asymptotic expression (25) can never be reached in the vicinity of the shock, because at these locations, the near field can not be neglected. This near field was not included in Ribner's calculations for the case of a shock/vortex interaction.

In a recent paper, Grasso and Pirozzoli[31] (GP) studied, both analytically and numerically, the sound generation resulting from a shock/spot interaction. They conducted two analytic developments of this problem. The first one is a semianalytical model, which applies in the limit of weak shocks. The second is an acoustic analogy that applies in the limit of either weak shocks or weak spot amplitudes. This second model may be compared to our linear solution. In Appendix D we reproduce GP's acoustic analogy for the case of a Gaussian spot with a weak amplitude ϵ. It is shown that in the limit $R/a\gg1$, their result can be set to a form similar to our expression (25),

$$\frac{p'}{P_2}\approx\frac{\epsilon}{\pi}\sqrt{\frac{2a}{R}}\mathbf{F}_{\mathrm{GP}}(\phi;M_1)\tilde{K}\left(\frac{r-R}{b'}\right), \tag{28}$$

where the function $\tilde{K}$ is the same than ours and where the length b' is given by Eq. (D17). The function $\mathbf{F}_{\mathrm{GP}}(\phi;M_1)$ describing the angular amplitude of the wave predicted by GP's acoustic analogy is given by Eq. (D15). This function is plotted in Fig. 15 for $M_1=1.2$ and $M_1=2$ and compared to the function $\mathbf{F}(\phi;M_1)$ obtained from the linear solution. It can be seen that on the downstream propagating parts of the wave ($0<\phi<90°$), GP's acoustic analogy and our linear solution are comparable, and that agreement is better for $M_1=1.2$ than for $M_1=2$. On the other hand, on the upstream propagating parts of the wave ($90°<\phi<\alpha_c^p$), for both cases $M_1=1.2$ and $M_1=2$, the acoustic levels predicted by GP's acoustic analogy are much greater than those predicted by our linear solution.

We expect our linear solution to be more accurate because it includes all the details of the interaction, whereas GP's acoustic analogy makes the hypothesis that the shock remains straight during the interaction. Also, GP's acoustic analogy predicts an acoustic emission in an unbounded medium, and it needs to be corrected to account for the acoustic

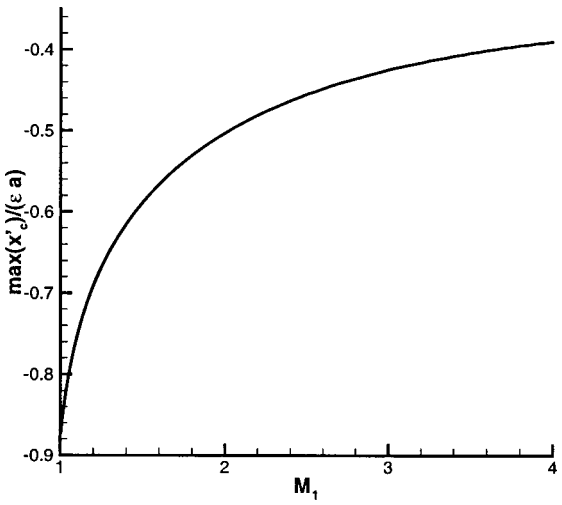

FIG. 16. Maximum shock deformation as a function of the shock Mach number.

waves reflected by the shock. For this later point, GP have shown that on the symmetry axis this correction is at most 4% for $M_1=2$, but it may be greater on the upstream propagating parts of the wave.

D. Shock displacement

The shock displacement given by Eq. (15) is represented in Fig. 12 at three different instants, for $M_1=2$. The maximum value of the shock displacement is reached approximately for the instant $R/a=1$, when the transmitted spot has completely emerged from the shock. Later, the shock front deformation widens, and its maximum amplitude seems to decrease as t^{-1}. It has also been verified that for $R/a<0$, corresponding to instants before the interaction, the shock displacement predicted by Eq. (15) quickly tends to zero. This means that our expressions respect the causality of the interaction.

The maximum displacement of the shock front during the interaction has been plotted as a function of the Mach number in Fig. 16. The shock displacement due to the interaction appears to be larger for weak shocks.

V. COMPARISON WITH A NUMERICAL SIMULATION

The linear solution developed herein is particularly suited for a comparison with numerical simulation results. Here we use a code based on a characteristic formulation of the Euler equations, as well as a shock-fitting technique to resolve the shock front.[33] We first give an outline of the numerical method, and then present comparisons of numerical results with the linear solution for $M_1=2$ and 4. This allows to demonstrate the validity of the linear theory when considering linear spot amplitudes, and to investigate the nature of the interaction when considering nonlinear spot amplitudes. For this latter point, the results presented herein complements those of Hussaini and Erlebacher.[30]

TABLE I. Convergence of numerical simulation results: Effect of mesh size ($M_1=2$, $R/a=4$).

	$\Delta x=0.16a$, $\Delta y=0.32a$	$\Delta x=0.08a$, $\Delta y=0.16a$	$\Delta x=0.04a$, $\Delta y=0.08a$	Theory
Min. pressure	−0.1026 <1%	−0.1024 <1%	−0.1025 <1%	−0.1024
Max. vorticity	2.029 5%	2.114 1%	2.129 <1%	2.131

A. Description of the numerical method

The idea of the code is based on the λ-scheme by Moretti,[34] and is ''refurbished and put to work'' with a high order compact upwind scheme and a Runge–Kutta time integration. Here, we just want to give a rough idea of the code and present the basics for a one-dimensional model problem. For a detailed description, please see Ref. 33.

The Euler equations in one space dimension can be regarded as three transport equations for two Riemann variables, $R^{\pm}=u\pm[2/(\gamma-1)]c$ and the entropy s. They take the form

$$\left(\frac{\partial R^{\pm}}{\partial t}-\frac{c}{\gamma\mathcal{R}}\frac{\partial s}{\partial t}\right)+(u\pm c)\left(\frac{\partial R^{\pm}}{\partial x}-\frac{c}{\gamma\mathcal{R}}\frac{\partial s}{\partial x}\right)=0, \tag{29}$$

$$\frac{\partial s}{\partial t}+u\frac{\partial s}{\partial x}=0. \tag{30}$$

These equations can be rearranged to express the time derivatives of the primitive variables,[33]

$$\frac{\partial p}{\partial t}=-\frac{\rho c}{2}[X^{+}+X^{-}]+\frac{p}{C_v}\left(\frac{\partial s}{\partial t}+X^{s}\right), \tag{31}$$

$$\frac{\partial u}{\partial t}=-\frac{1}{2}[X^{+}-X^{-}], \tag{32}$$

$$\frac{\partial s}{\partial t}=-X^{s}, \tag{33}$$

where the following notation has been introduced:

$$X^{\pm}=(u\pm c)\left(\frac{\partial R^{\pm}}{\partial x}-\frac{c}{\gamma\mathcal{R}}\frac{\partial s}{\partial x}\right)=(u\pm c)\left(\frac{1}{\rho c}\frac{\partial p}{\partial x}\pm\frac{\partial u}{\partial x}\right), \tag{34}$$

$$X^{s}=u\frac{\partial s}{\partial x}. \tag{35}$$

Each of the space derivatives $X^{\pm}$, X^{s} is uniquely related to a propagation direction which is either $u\pm c$ or u. We can construct a stable numerical scheme for the set of equations [(31)–(33)] by choosing an upwind differentiation with respect to the sign of the propagation direction for each of these terms. In our case, we have used a fifth order compact upwind scheme[35] for the space derivatives, and a low storage third order Runge–Kutta scheme[36] for time advancement. Please note that the continuity equation (31) might be simplified by Eq. (33), but this is only possible for isentropic flows. In the computation of viscous flows, one has to keep it as it stands.

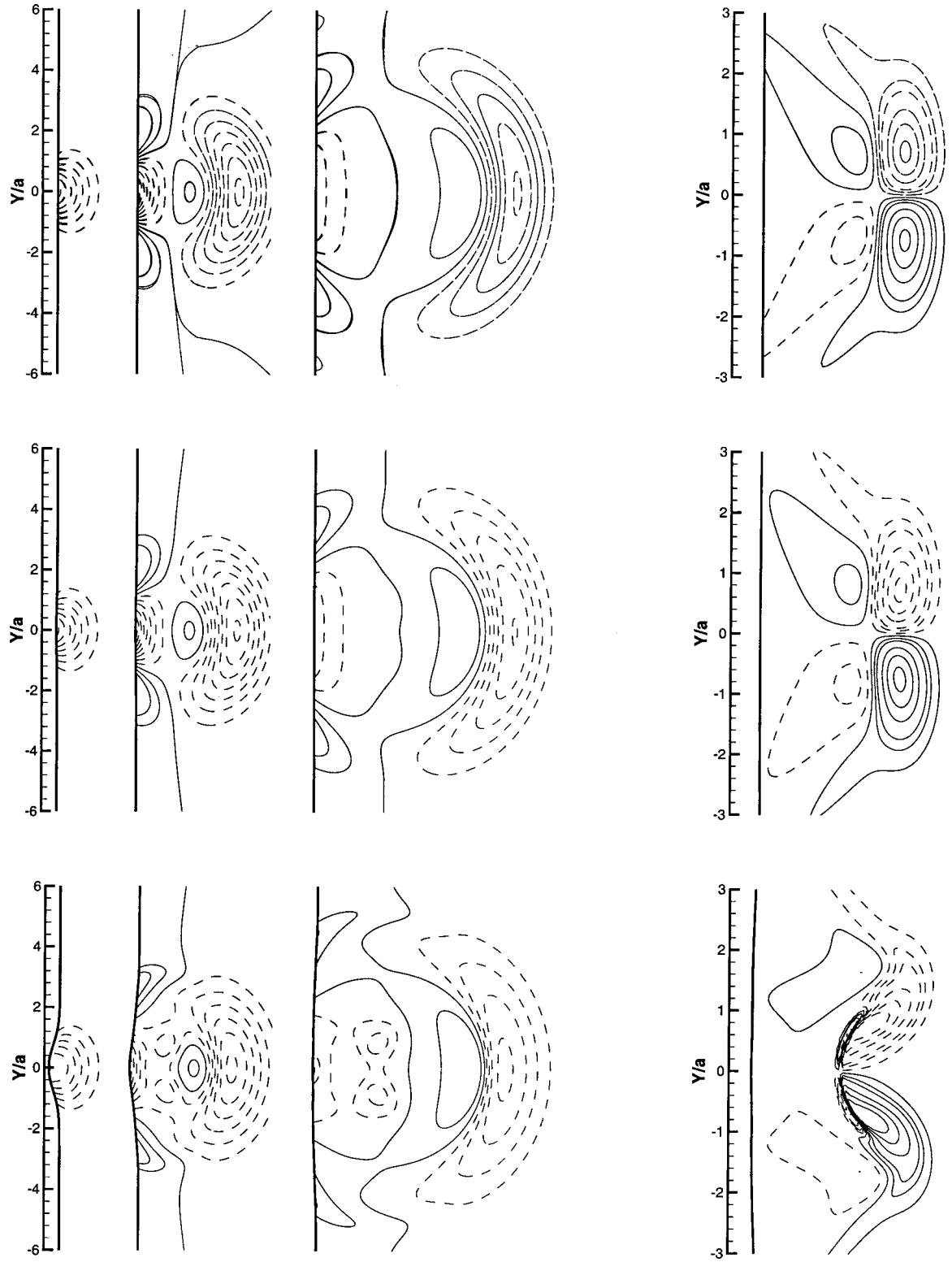

FIG. 17. Vorticity and pressure fields for $M_1=2$. Upper plots: superposition of linear theory and numerical simulation with $\epsilon=10^{-2}$. Middle plots: numerical simulation with $\epsilon=10^{-1}$. Lower plots: numerical simulation with $\epsilon=1$. For each case, from left to right: pressure field for three different instants corresponding to $R/a=0$, 2, and 4, and vorticity field at instant corresponding to $R/a=4$. Pressure levels are as in Fig. 12, and vorticity levels are as in Fig. 10.

For two space dimensions, there exists no equivalent formulation in terms of a finite number of Riemann variables because the two acoustic characteristics corresponding to $X^{\pm}$ are degenerated from an infinite number of characteristics. But it is straightforward to decompose the equations formally in the same way for the y direction and also for time-dependent arbitrary grids. A set of equations generalizing the system (31)–(33) can be obtained, see Ref. 33, Eq. (42).

The resulting scheme is not conservative. Thus we cannot capture shocks. (In practice, the scheme proves to be

TABLE II. Comparison between linear theory and numerical simulation for $M_1=2$, $R/a=0$.

	Theory	$\epsilon=10^{-4}$	$\epsilon=10^{-2}$	$\epsilon=10^{-1}$	$\epsilon=1$
Min. pressure	−0.3757	−0.3768 <1%	−0.3762 <1%	−0.3710 <1%	−0.3080 <18%
Max. vorticity	2.128	2.125 <1%	2.126 <1%	2.148 <1%	2.248 <6%
Max. entropy	0.9327	0.9369 <1%	0.9370 <1%	0.9372 <1%	0.9527 <2%
Max. deformation	−0.2932	−0.2931 <1%	−0.2938 <1%	−0.2936 <1%	−0.3603 <23%

TABLE IV. Comparison between linear theory and numerical simulation for $M_1=4$, $R/a=0$.

	Theory	$\epsilon=10^{-4}$	$\epsilon=10^{-2}$	$\epsilon=10^{-1}$	$\epsilon=1$
Min. pressure	−0.5162	−0.5187 <1%	−0.5175 <1%	−0.5071 2%	−0.4014 22%
Max. vorticity	5.566	5.549 <1%	5.552 <1%	5.575 <1%	5.919 6%
Max. entropy	0.7519	0.7553 <1%	0.7554 <1%	0.7563 <1%	0.7789 4%
Max. deformation	−0.2218	−0.2216 <1%	−0.2219 <1%	−0.2250 <2%	−0.2570 15%

robust enough to handle moderate shocks anyhow.[33]) Strong shocks need to be fitted. We follow the idea of Moretti,[37] see, e.g., Erlebacher *et al.*[38] The grid is time dependent and the shock is taken to be the left, moving boundary. The other boundaries are taken to be nonreflecting. According to characteristic theory, four characteristics (in two space dimensions) enter the shock from the left and one from the computational domain. Given this information, it is possible (though tedious) to compute X^+, X^s, and $X^v=u(\partial v/\partial x)$, as well as the shock acceleration.[38] This information actually forms the numerical boundary condition which the scheme ''sees.'' The shock location and velocity are advanced in time with the same Runge–Kutta scheme as the flow field, and the grid is deformed to follow the shock deformation.

B. Results

At first, we have validated the code's convergence by performing simulations with different mesh sizes. The dimensions of the computational domain, initially rectangular, were $-10a<y<10a$ and $0<x<10a$. We used a coarse grid ($\Delta x=0.16a$, $\Delta y=0.32a$), an intermediate one ($\Delta x=0.08a$, $\Delta y=0.16a$), and a refined one ($\Delta x=0.04a$, $\Delta y=0.08a$). The Mach number was $M_1=2$ and the spot's amplitude was set to $\epsilon=10^{-4}$, in order to remain within the limits of validity of the linear solution. The extremum values of the pressure and the vorticity, deduced from the numerical simulations at a nondimensional time $R/a=4$, are reported in Table I and compared to the linear solution. As it can be seen, when considering the pressure field, the coarse grid is sufficient to obtain a good convergence of the numerical simulation toward the linear solution. However, the vorticity field, a quantity which is more dependent upon the discretization, needs a refined grid to converge toward the linear solution.

We performed a series of computations to study the validity of the linear solution with regards to the amplitude ϵ of the incident spot. We used the refined grid specified above. The amplitude ϵ was set to 10^{-4}, 10^{-2}, 10^{-1}, and 1. We considered two cases with Mach numbers of $M_1=2$ and 4.

Figure 17 shows computation results for $M_1=2$. We have represented the pressure levels for three instants corresponding to $R/a=0$, 2, and 4, and the vorticity field corresponding to the last of these instants. The upper plots are a superposition of the linear solution and of the numerical results with $\epsilon=10^{-2}$. As it can be seen, for the vorticity field, both plots are not distinguishable from each other. For the pressure levels, very small differences are found, in particular for the level corresponding to zero, which is not correctly resolved, and for the pressure in the near field (the parts of the field close to the shock front). However, concerning the near field, the difference does not correspond to a bad accordance between the linear solution and the numerical simulation, but rather to a difficulty in evaluating the double integral in Eq. (14).

TABLE III. Comparison between linear theory and numerical simulation for $M_1=2$, $R/a=4$.

	Theory	$\epsilon=10^{-4}$	$\epsilon=10^{-2}$	$\epsilon=10^{-1}$	$\epsilon=1$
Min. pressure	−0.1024	−0.1025 <1%	−0.1024 <1%	−0.1010 1%	−0.0854 17%
Max. pressure	0.0632	0.0632 <1%	0.0630 <1%	0.0607 4%	0.0418 33%
Max. vorticity	2.131	2.129 <1%	2.134 <1%	2.164 2%	2.773 30%
Max. entropy	0.931	0.937 <1%	0.936 <1%	0.939 <1%	0.934 <1%
Max. deformation	−0.1782	−0.1783 <1%	−0.1782 <1%	−0.1774 <1%	−0.1345 24%

TABLE V. Comparison between linear theory and numerical simulation for $M_1=4$, $R/a=4$.

	Theory	$\epsilon=10^{-4}$	$\epsilon=10^{-2}$	$\epsilon=10^{-1}$	$\epsilon=1$
Min. pressure	−0.1809	−0.1811 <1%	−0.1807 <1%	−0.1764 3%	−0.1306 28%
Max. pressure	0.0746	0.0747 <1%	0.0749 <1%	0.0763 2%	0.1230 65%
Max. vorticity	5.566	5.556 <1%	5.549 <1%	5.702 <2%	8.760 57%
Max. entropy	0.7519	0.7518 <1%	0.7569 <1%	0.7591 <1%	0.7162 4%
Max. deformation	−0.1212	−0.1213 <1%	−0.1212 <1%	−0.1198 <1%	−0.1014 16%

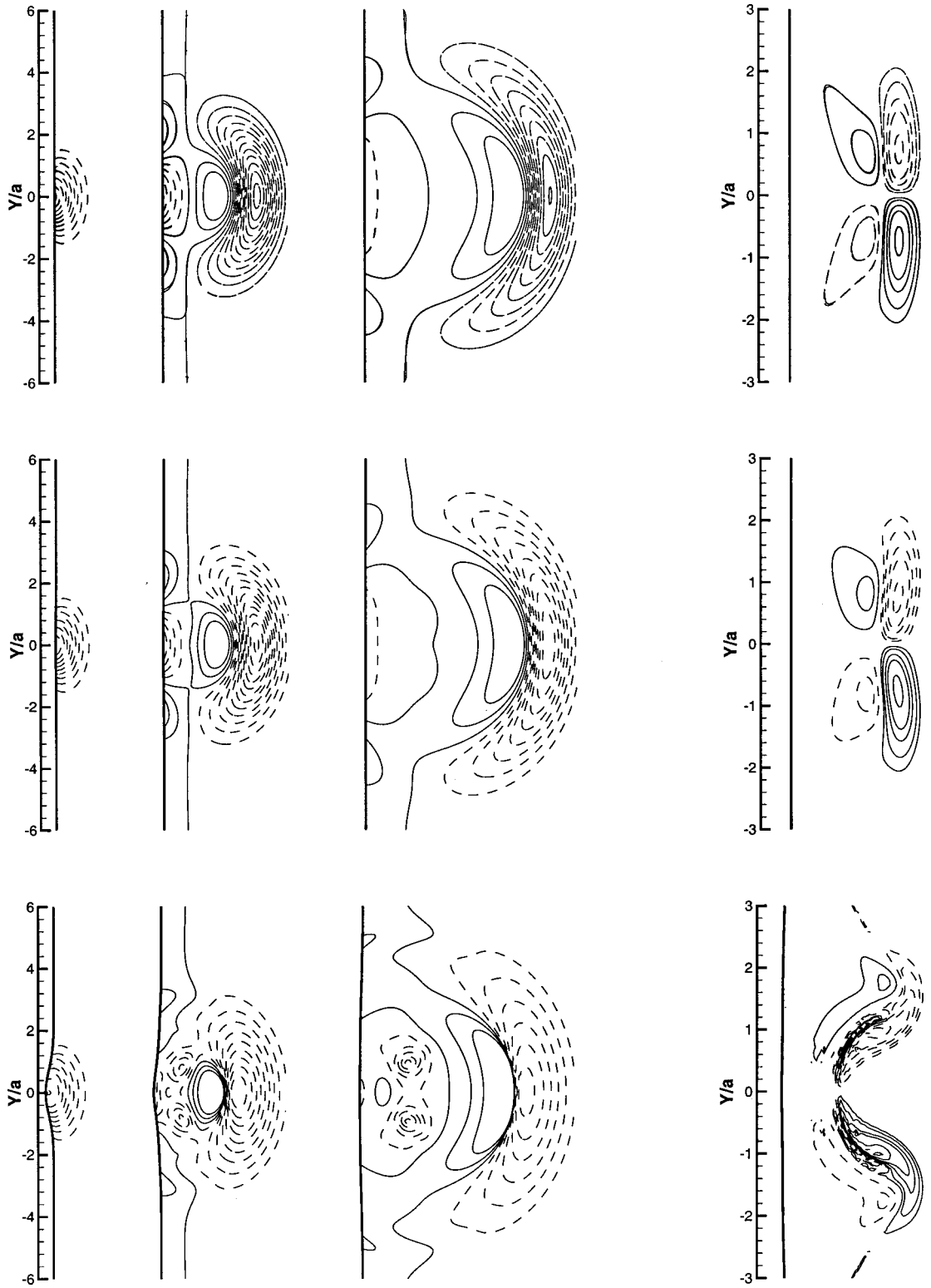

FIG. 18. Vorticity and pressure fields for $M_1=4$. Upper plots: superposition of linear theory and numerical simulation with $\epsilon=10^{-2}$. Middle plots: numerical simulation with $\epsilon=10^{-1}$. Lower plots: numerical simulation with $\epsilon=1$. For each case, from left to right: pressure field for three different instants corresponding to $R/a=0$, 2, and 4, and vorticity field at instant corresponding to $R/a=4$. Pressure levels are as in Fig. 12, and vorticity levels correspond to ± 0.5, 1, 1.5, 2, 3, 5, 8.

The middle and lower plots represent the same data from the numerical simulations with $\epsilon=10^{-1}$ and 1. For $\epsilon=10^{-1}$, very little differences are found. For $\epsilon=1$, nonlinear effects are clearly visible. Considering the vorticity field, it is observed that the vortices are highly distorted, due to their self-induced roll-up. Considering the pressure field, one observes a low pressure region in the center of the acoustic wave. This corresponds to the nonlinear pressure deficit as-

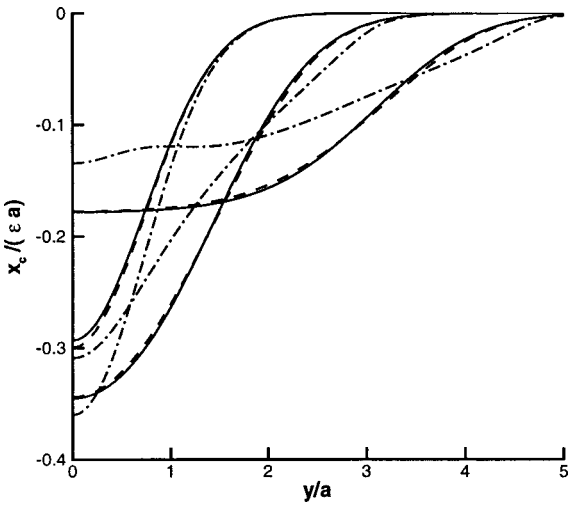

FIG. 19. Shock deformation $x_c'/\epsilon a$ for $M_1=2$, at three different instants corresponding to $R/a=0$, 2, and 4. Linear theory (full lines), $\epsilon=10^{-1}$ (dashed lines), $\epsilon=1$ (dotted lines).

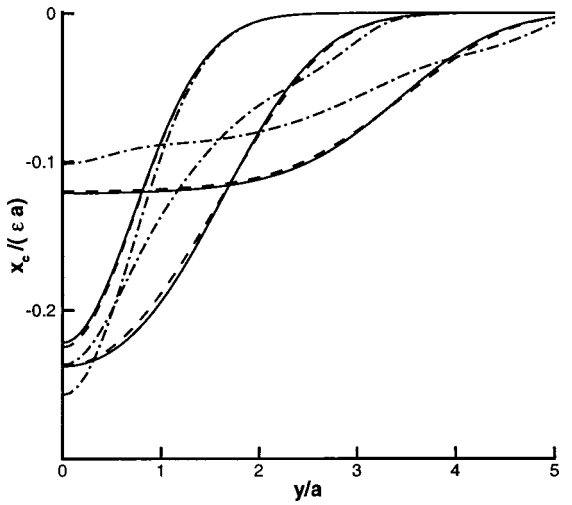

FIG. 20. Shock deformation $x_c'/\epsilon a$ for $M_1=4$, at three different instants corresponding to $R/a=0$, 2, and 4. Linear theory (full lines), $\epsilon=10^{-1}$ (dashed lines), $\epsilon=1$ (dotted lines).

sociated with the vortices. One also observes that the pressure levels in the front of the acoustic wave are tightened. This is due to the steepening of the acoustic wave. However the shape of the acoustic wave remains qualitatively the same.

Tables II and III display quantitative comparisons between the numerical computations and the linear solution. We have reported the extremum values of the pressure, the vorticity, the entropy and the shock displacement for the nondimensional times $R/a=0$ and 4. As can be seen, for the simulations with $\epsilon=10^{-4}$ and 10^{-2}, the difference with the linear solution is smaller than 1%. For the simulation with $\epsilon=10^{-1}$, the accordance with the linear solution is still excellent, differences being of the order of 1%. The greater difference is found for the maximum pressure at the instant corresponding to $R/a=4$. This is not surprising because this region corresponds to the contribution of the pressure components at the critical angles, where it is known that the LIA theory is less accurate.[16]

Considering the simulation with $\epsilon=1$, i.e., a true nonlinear case, it is striking to see that the reported values are still in good accordance with the theory. At the instant when the spot crosses the shock $(R/a=0)$, one only observes a 6% difference for the maximum vorticity, and a 2% difference for the maximum entropy. Other reported quantities differ of about 20%, which can still be regarded as a good accordance with the theory, considering that we have a 100% initial amplitude in the spot. At the instant corresponding to $R/a=4$, as the vortices roll up, the maximum vorticity strays from the theory, but the other quantities still remain close to the theory. In particular, it is found that the maximum of entropy perturbation relaxes to the theoretical prediction within 1%.

Figure 18 and Tables IV and V display the same results obtained from the $M_1=4$ computations. As for the $M_1=2$ case, the computations with $\epsilon=10^{-4}$, 10^{-2}, and 10^{-1} are in excellent agreement with the linear solution. For the $\epsilon=1$ case, the nonlinear effects are more intense. In particular, on observes that the steepening of the acoustic wave has lead to the apparition of a secondary shock wave. However, as reported by Table IV, at the instant $R/a=0$ corresponding to the initial stages of the interaction, the numerical simulation still keeps a correct accordance with the linear theory. This accordance deteriorates in the latter stages of the interaction (see Table V) as the nonlinear effects become predominant.

Finally, Figs. 19 and 20 compare the shock deformation from the linear theory and from the numerical simulations, respectively for $M_1=2$ and $M_1=4$. Again, it is observed that the simulation compares very favorably with the linear theory up to $\epsilon=10^{-1}$, and that for the $\epsilon=1$ case, the agreement deteriorates as time is increased.

The results presented in this section suggest that, even for large spot amplitudes, the shock–spot interaction is dominated by a linear mechanism, and that nonlinearities rather affect the pressure and vorticity fields in the postinteraction stages. These conclusions complement those of Hussaini and Erlebacher[30] who performed numerical simulations for $M_1=2$ and 10 and for spot amplitudes varying from $-0.25<\epsilon<0.25$, and concentrated on the nonlinear aspects of the interaction.

VI. THE CASE OF A CONSTANT ENTROPY SPOT

The method used in Sec. III for a Gaussian spot can be applied to spots with different profiles, provided that a Fourier decomposition of the profile is known. It is of interest to know how the actual spot profile influences the interaction. In this section, we will apply the LIA method to a ''tophat'' spot with a constant entropy value within its radius a. This constitutes a good model for a cylindrical bubble of a different gas carried through a shock.

A. Detailed calculation

The initial entropy perturbation is taken as

$$\frac{s_1'}{C_p}=\begin{cases}\epsilon & r<a,\\ 0 & r>a.\end{cases} \tag{36}$$

The corresponding Fourier transform and the ''slice'' decomposition are, respectively, given by

$$\frac{s_1'}{C_p}=\frac{\epsilon}{\pi}\int_0^{\pi}\int_0^{\infty}J_1(ka)e^{ik\hat{r}}d(ka)d\alpha, \tag{37}$$

$$\frac{s_1'}{C_p}=\frac{\epsilon}{\pi}\int_0^{\pi}K^c\left(\frac{\hat{r}}{a}\right)d\alpha. \tag{38}$$

Here, J_1 is the Bessel function of the first kind and of order 1, and the function K^C is given by a Weber–Shafheitlin discontinuous integral (see Ref. 32, p. 487),

$$K^C(z)=\begin{cases}1 & |z|<1,\\ \dfrac{-1}{z^2-1+|z|\sqrt{z^2-1}} & |z|>1.\end{cases} \tag{39}$$

The analysis can be carried out in a manner similar to that developed in Sec. III. The entropy, velocity and vorticity fields are given by Eqs. (8)–(11), where the functions K and L are replaced by the corresponding functions K^C and L^C. The function L^C is

$$L^C(z)=\begin{cases}\dfrac{z}{\sqrt{1-z^2}} & |z|<1,\\ 0 & |z|>1.\end{cases} \tag{40}$$

The pressure field is given by

$$\frac{p'}{P_2}=\frac{\epsilon}{\pi}\int_{-\alpha_c^p}^{\alpha_c^p}K^C\left(\frac{\hat{r}^p-R}{b}\right)Z_{sp}J^p d\alpha^p + \frac{\epsilon}{\pi}\int_{\alpha_c}^{\pi-\alpha_c}Z_{sp}d\alpha\int_0^{\infty}J_1(ka)e^{k^p(i\hat{\rho}-\eta(x-x_c))}d(ka), \tag{41}$$

and the shock deformation is obtained from Eq. (15), with the new profile functions

$$K^{CI}(z)=\begin{cases}\sqrt{1-z^2} & |z|<1,\\ 0 & |z|>1,\end{cases} \tag{42}$$

$$L^{CI}(z)=\begin{cases}z & |z|<1,\\ \dfrac{1}{z+\mathrm{sgn}(z)\sqrt{z^2-1}} & |z|>1.\end{cases} \tag{43}$$

B. Results

Some difficulties arise when evaluating the different components of the flow field because the functions entering the analysis are discontinuous with infinite branches and integral expressions such as Eq. (41) do not converge numerically. As a consequence, this section primarily presents qualitative results.

1. Vorticity field

The vorticity field consists of two parts. The first part is singular, and corresponds to a vortex sheet located on the interface of the transmitted spot. The second part is regular, and is located within the transmitted spot. An important consequence is that the vorticity levels are far more important than for a Gaussian spot. They are theoretically infinite and-consequently, the spot will roll up much more rapidly. This can be observed in the numerical simulations of Picone and Boris,[27] which showed a rapid roll-up after the interaction. The expression (18) for the circulation of the vortices is still valid, but the value of the form factor f has to be set to 1 instead of $\sqrt{\pi}/2$ (see Appendix B). Thus the expression proposed by Yang *et al.* and presented in Sec. IV B is exactly retrieved.

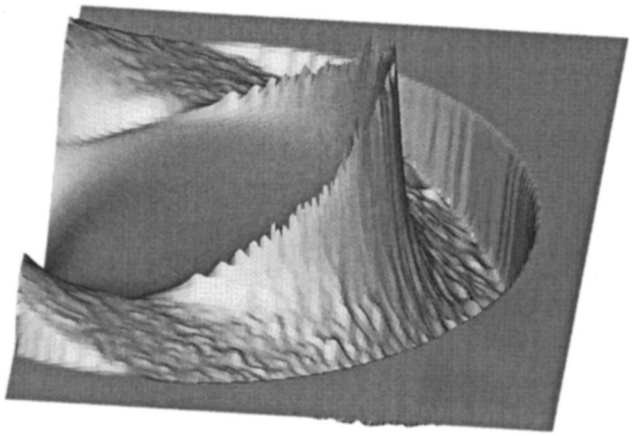

FIG. 21. Pressure field resulting from the interaction of a constant spot with a $M_1=2$ shock ($R/a=4$).

2. Pressure field

The pressure field is plotted in Fig. 21 for a $M_1=2$ shock, and for the instant corresponding to $R/a=4$. Due to the problems of convergence evoked above, Fig. 21 is not very accurate. However, it allows a qualitative description of the pressure field. As for the Gaussian spot, the pressure field is composed of a double cylindrical wave with a dipolar structure, and a low pressure near field above the shock. But the pressure variations are sharper than for the Gaussian spot.

One can still use the asymptotic expression given by Eq. (25), but the function $\tilde{K}(z)$ must be replaced by

$$\tilde{K}^C(z)=\int_0^{\infty}\frac{1}{\sqrt{z'}}K^C(z-z')dz'.$$

This function is plotted in Fig. 14. It contains a jump at $z=1$, and a logarithmic singularity at $z=-1$. So, as for the vorticity, the pressure field theoretically reaches infinite values, whatever the initial amplitude of the spot. As a consequence, nonlinear effects are likely to be important, even for weak initial spot amplitudes.

VII. SUMMARY

In this paper, we have used Ribner's linear interaction analysis (LIA) theory to solve the problem of a cylindrical entropy spot of weak amplitude convected through a shock wave. The interaction leads to a transmitted spot, a pair of counter-rotating vortices, a cylindrical sound wave, and a deformation of the shock front.

The method was first applied to a Gaussian entropy spot. An exhaustive description of the solution has been given for a Mach 2 shock, and the flow field has been characterized for a wide range of Mach numbers. An expression for the circulation of the vortices has been given as a function of the shock strength. This expression was shown to be in accordance with the numerical computations and qualitative predictions of Yang *et al.*[29] An asymptotic expression for the pressure in the cylindrical acoustic wave has also been developed and compared to a recent model given by Grasso and Pirozzoli.[31]

The linear solution has been compared to a numerical simulation result. Excellent qualitative and quantitative agreement was obtained, even for large spot amplitudes. This indicates that the features of the interaction are essentially linear.

Finally, the analytical method has been applied to a constant entropy spot, which is a model for a bubble of light gas carried by the flow. The interaction consists of the same phenomena, but the vorticity and pressure fields contain singularities. As a result, nonlinear effects are expected to be more important than for a Gaussian spot.

APPENDIX A: LINEAR INTERACTION ANALYSIS (LIA) FOR PLANE WAVES

In this appendix, we consider the LIA problem for plane elementary waves convected through a shock. As said in the Introduction, several solutions of this problem have been given with different methods. Ribner[2] treated the case of incident vorticity waves. Moore[3] solved the problem for incident acoustic waves. The solution of the problem for incident entropy waves was then given by Chang.[4] Here we propose a general form for the transfer functions which applies for the three kinds of incident waves.[39] These transfer functions may be used to study the interaction of perturbation fields combining the three modes of fluctuations with shocks. An application to different cases of homogeneous perturbation fields is given in Ref. 40.

1. Formulation for an entropy wave convected through a shock

We consider the interaction of a plane elementary entropy wave with a shock, as represented in Figs. 2 and 3. The origin of the frame is located on the unperturbed shock front, and we define the coordinates in the directions α, α^s, and α^p as

$$\hat{r}=x\cos\alpha+y\sin\alpha,$$

$$\hat{\sigma}=x\cos\alpha^s+y\sin\alpha^s,$$

$$\hat{\rho}=x\cos\alpha^p+y\sin\alpha^p.$$

All the angles considered belong to $[0,\pi]$.

We suppose that the upstream perturbation field consists of an elementary entropy wave of wavelength $2\pi/k$, angle α, and amplitude ϵ. This takes the form (for $x<0$)

$$\frac{s_1'}{C_p}=\epsilon e^{ik\hat{r}-i\omega t}, \tag{A1}$$

where the real part is to be retained. This plane wave is superposed to a main flow field with pressure P_1, density ρ_1, and velocity U_1. The condition that the entropy wave is convected with the mean flow simply reads

$$\omega=kU_1\cos\alpha. \tag{A2}$$

The downstream ($x>0$) flow field is searched as a mean field of velocity U_2, density ρ_2, and pressure P_2 plus perturbations.

The mean field is determined by the classical Rankine–Hugoniot jump relations. In particular, the downstream Mach number M_2, the compression rate $m=\rho_2/\rho_1=U_1/U_2$, and the pressure jump P_2/P_1 can be expressed as functions of the upstream Mach number M_1,

$$m=\frac{(\gamma+1)M_1^2}{2+(\gamma-1)M_1^2}, \tag{A3}$$

$$M_2=\sqrt{\frac{2+(\gamma-1)M_1^2}{2\gamma M_1^2-(\gamma-1)}}, \tag{A4}$$

$$P_2/P_1=1+\frac{2\gamma}{\gamma+1}(M_1^2-1). \tag{A5}$$

The ratio of specific heats of the gas is $\gamma=1.4$ throughout this work.

As represented in Figs. 2 and 3, the entropy and solenoidal velocity perturbations generated downstream are considered as plane waves of angle α^s and wavelength $2\pi/k^s$. The pressure field is considered as a ''generalized'' pressure wave with amplitude proportional to $e^{ik^p\hat{\rho}}e^{-k^p\eta x}$. This represents a perturbation with a constant phase in the direction α^p, but with an amplitude that may decay away from the shock. The parameter η characterizes the decay rate; one wavelength downstream of the shock, the amplitude of the perturbation is damped by a factor $e^{-2\pi\eta}$.

According to the angle α of the incident entropy wave, this generalized wave may have a propagative nature ($\eta=0$, see Fig. 2) or a nonpropagative nature ($\eta\neq0$, see Fig. 3).

We denote by Z_{ss}, Z_{sv}, and Z_{sp} the relative amplitudes of the entropy, vorticity, and pressure waves. We also suppose that the shock front deforms with an amplitude Z_{sx}. These amplitudes may be complex. In that case, the real part represents the component of the wave in phase with the incident wave, and the imaginary part represents the component in phase quadrature.

So the perturbation field is searched as (for $x>0$)

$$\frac{s'}{C_p}=\epsilon Z_{ss}e^{ik^s\hat{\sigma}-i\omega t},$$

$$\frac{p'}{P_2}=\epsilon Z_{sp}e^{k^p(i\hat{\rho}-\eta x)-i\omega t},$$

$$\frac{u'}{U_2}=\epsilon\sin\alpha^s Z_{sv}e^{ik^s\hat{\sigma}-i\omega t}+\frac{\cos\alpha^p+i\eta}{\gamma M_2\xi}\frac{p'}{P_2},$$

$$\frac{v'}{U_2}=-\epsilon\cos\alpha^s Z_{sv}e^{ik^s\hat{\sigma}-i\omega t}+\frac{\sin\alpha^p}{\gamma M_2\xi}\frac{p'}{P_2}, \tag{A6}$$

$$\frac{\rho'}{\rho_2}=\frac{1}{\gamma}\frac{p'}{P_2}-\frac{s'}{C_p},$$

$$\frac{\theta'}{T_2}=\frac{\gamma-1}{\gamma}\frac{p'}{P_2}+\frac{s'}{C_p},$$

$$kx_c'=\epsilon Z_{sx}e^{ik\sin\alpha y-i\omega t}.$$

In the expressions for the velocity perturbation, the first and second term in the right-hand side correspond to the solenoidal and potential velocity fluctuations, respectively. The function ξ appearing in the potential velocity fluctuation is 1 in the propagative regime, and it is complex, and given by

$$\xi=\sqrt{1-\eta^2+2i\eta\cos\alpha^p} \tag{A7}$$

in the nonpropagative regime $(-\pi/2\leqslant\arg\xi\leqslant 0)$. This means that in a nonpropagative generalized pressure wave, the irrotational velocity fluctuation is not in phase with the pressure fluctuation contrary to a classical acoustic wave.

The geometrical characteristics of the resulting waves are determined by the requirement that, on the shock front, the y and temporal dependencies of these waves match with those of the incident wave.

For the entropy and vorticity waves, this leads to

$$\cot\alpha^s=m\cot\alpha, \tag{A8}$$

$$k^s/k=\sin\alpha/\sin\alpha^s. \tag{A9}$$

For the pressure wave, the solution of the propagative regime differs from that of the nonpropagative regime. The limiting angle between the propagative and nonpropagative regimes is α_c. The resulting entropy and vorticity waves exhibit the angle α_c^s, and the resulting pressure wave exhibits the angle α_c^p. These critical angles are given by

$$\cot\alpha_c=\frac{\sqrt{1-M_2^2}}{mM_2},\quad \sin\alpha_c^s=M_2,\quad \cos\alpha_c^p=-M_2. \tag{A10}$$

In the propagative regime $(0<\alpha<\alpha_c)$, $\eta=0$, and the angles α and α^p are related by

$$\frac{\cot\alpha^p}{\cot\alpha_c^p}=\frac{\cot\alpha}{\cot\alpha_c}-\frac{1}{M_2}\sqrt{\left(\frac{\cot\alpha}{\cot\alpha_c}\right)^2-1}, \tag{A11}$$

or, equivalently,

$$m\cot\alpha=\cot\alpha^p+\frac{1}{M_2\sin\alpha^p}. \tag{A12}$$

In the nonpropagative regime $(\alpha_c<\alpha<\pi/2)$, the angle α^p and the decay rate η are given by

$$\frac{\cot\alpha^p}{\cot\alpha_c^p}=\frac{\cot\alpha}{\cot\alpha_c}, \tag{A13}$$

$$\eta=\frac{|\cot\alpha_c^p\sin\alpha^p|}{M_2}\sqrt{1-\left(\frac{\cot\alpha}{\cot\alpha_c}\right)^2}. \tag{A14}$$

In both regimes, $0\leqslant\alpha^p<\pi$, and the wavelength of the generalized pressure wave is given by

$$k^p/k=\sin\alpha/\sin\alpha^p. \tag{A15}$$

Finally, the Jacobians $J^s=\partial\alpha/\partial\alpha^s$ and $J^p=\partial\alpha/\partial\alpha^p$, which are needed for the evaluation of the expressions in Sec. III, are given by

$$J^s=\frac{m(1+\tan^2\alpha^s)}{1+m^2\tan^2\alpha^s}, \tag{A16}$$

$$J^p=\frac{1+\cot^2\alpha^p}{m(1+\cot^2\alpha)}\left(1+\frac{\cos\alpha^p}{M_2}\right). \tag{A17}$$

We now substitute the perturbation field described by the set of expressions (A6) into the jump relations at the shock front (conservation of mass, normal and tangential momentum and energy). We retain the terms proportional to ϵ. This results in a linear system which takes the following form:

$$[\mathcal{A}]\begin{bmatrix}Z_{sv}\\Z_{ss}\\Z_{sp}\\Z_{sx}\end{bmatrix}=\begin{bmatrix}-1\\-m\\0\\\dfrac{m^2}{(\gamma-1)M_1^2}\end{bmatrix}, \tag{A18}$$

where the matrix $[\mathcal{A}]$ is given by

$$[\mathcal{A}]=\begin{bmatrix}\sin\alpha^s & -1 & \dfrac{1}{\gamma}+\dfrac{\cos\alpha^p+i\eta}{\gamma M_2\xi} & i(m-1)\cos\alpha\\ 2\sin\alpha^s & -1 & \dfrac{M_2^2+1}{\gamma M_2^2}+2\dfrac{\cos\alpha^p+i\eta}{\gamma M_2\xi} & 0\\ -\cos\alpha^s & 0 & \dfrac{\sin\alpha^p}{\gamma M_2\xi} & i(1-m)\sin\alpha\\ \sin\alpha^s & \dfrac{1}{(\gamma-1)M_2^2} & \dfrac{1}{\gamma M_2^2}+\dfrac{\cos\alpha^p+i\eta}{\gamma M_2\xi} & im(1-m)\cos\alpha\end{bmatrix}. \tag{A19}$$

Inversion of the above system allows the determination of the amplitudes of the different transmitted waves. The solution is consistent with the one given by Chang.[4]

2. Formulation for an incident vorticity wave

The formulation given above can easily be adapted for the problem of an incident vorticity wave, initially studied by Ribner.[2] Upstream we impose

$$\frac{u_1'}{U_1} = \epsilon \sin\alpha e^{ik\hat{r}-i\omega t},$$

$$\frac{v_1'}{U_1} = -\epsilon \cos\alpha e^{ik\hat{r}-i\omega t},$$

with ω given by Eq. (A2). Downstream we set a decomposition similar to that given by (A6), but with amplitudes Z_{vs}, Z_{vv}, Z_{vp}, and Z_{vx}. These amplitudes are found as the solutions of the linear system,

$$[\mathcal{A}]\begin{bmatrix} Z_{vv} \\ Z_{vs} \\ Z_{vp} \\ Z_{vx} \end{bmatrix} = \begin{bmatrix} \sin\alpha \\ 2m\sin\alpha \\ -m\cos\alpha \\ m^2\sin\alpha \end{bmatrix}. \tag{A20}$$

Note that we chose to nondimensionalize the upstream velocity amplitudes with U_1 and the downstream velocity amplitudes with U_2. So the transfer function for dimensional velocity amplitudes is Z_{vv}/m.

3. Formulation for an incident acoustic wave

The interaction problem for an incident acoustic wave, first solved by Moore,[3] is a bit more complicated. Upstream incident pressure waves can be classified in two types: the ''fast waves'' which propagate in the direction of the mean flow, and the ''slow waves,'' which propagate in the opposite direction. The limit between these two types are the stationary Mach waves, which are characterized by the angle $\alpha_M = \cos^{-1}(-1/M_1)$. The interaction of both types of waves can be propagative or nonpropagative. The limiting angles are α_{cl} and α_{cu}. These angles are the solutions of[3]

$$\cot\alpha + \frac{1}{M_1\sin\alpha} = \pm\frac{\sqrt{1-M_2^2}}{mM_2}. \tag{A21}$$

This problem can still be solved with the method developed above. Let us consider an incident acoustic wave of amplitude ϵ and angle α taken in the range $[0,\pi]$, i.e., $p_1'/P_1 = \epsilon\exp(ik\hat{r}-i\omega t)$, with $\omega = kU_1(\cos\alpha + 1/M_1)$. The downstream solution is searched as a decomposition similar to that given by (A6), but with amplitudes Z_{ps}, Z_{pv}, Z_{pp}, and Z_{px}.

In order to simplify the geometrical relations we introduce the angle α' of the entropy or vorticity wave that would have the same y and temporal dependencies than the incident acoustic wave. α' is given by

$$\cot\alpha' = \cot\alpha + \frac{1}{M_1\sin\alpha}, \quad (0 \leqslant \alpha' \leqslant \pi). \tag{A22}$$

The angle α^s of the resulting entropy and vorticity waves is given by Eq. (A8), where α is replaced by α'. The solution for α^p is different for fast and slow incident waves.

(a) For a fast wave in the propagative regime ($0 < \alpha < \alpha_{cl}$):

$$\frac{\cot\alpha^p}{\cot\alpha_c^p} = \frac{\cot\alpha'}{\cot\alpha_c} - \frac{1}{M_2}\sqrt{\left(\frac{\cot\alpha'}{\cot\alpha_c}\right)^2 - 1}, \tag{A23}$$

with $0 < \alpha^p < \pi$.

(b) For a fast wave in the nonpropagative regime ($\alpha_{cl} < \alpha < \alpha_M$):

$$\frac{\cot\alpha^p}{\cot\alpha_c^p} = \frac{\cot\alpha'}{\cot\alpha_c}, \tag{A24}$$

with $0 < \alpha^p < \pi$.

(c) For a slow wave in the nonpropagative regime ($\alpha_M < \alpha < \alpha_{cu}$):

$$\frac{\cot\alpha^p}{\cot\alpha_c^p} = \frac{\cot\alpha'}{\cot\alpha_c}, \tag{A25}$$

with $\pi < \alpha^p < 2\pi$.

(d) For a slow wave in the propagative regime ($\alpha_{cu} < \alpha < \pi$):

$$\frac{\cot\alpha^p}{\cot\alpha_c^p} = \frac{\cot\alpha'}{\cot\alpha_c} + \frac{1}{M_2}\sqrt{\left(\frac{\cot\alpha'}{\cot\alpha_c}\right)^2 - 1}, \tag{A26}$$

with $\pi < \alpha^p < 2\pi$.

The change in the determination of α^p accounts for the reverse in the direction of propagation from the fast waves to the slow waves. The decay rate in the nonpropagative regimes is given by Eq. (A14), where α is replaced by α'. The wavelengths of the waves are still given by Eqs. (A9) and (A15).

Finally, the amplitudes of the generated waves are found by solving

$$[\mathcal{A}]\begin{bmatrix} Z_{pv} \\ Z_{ps} \\ Z_{pp} \\ \dfrac{\sin\alpha}{\sin\alpha'}Z_{px} \end{bmatrix} = \begin{bmatrix} \dfrac{1}{\gamma} + \dfrac{\cos\alpha}{\gamma M_1} \\ \dfrac{m}{\gamma}\left(\dfrac{M_1^2+1}{M_1^2} + \dfrac{2\cos\alpha}{M_1}\right) \\ \dfrac{m\sin\alpha}{\gamma M_1} \\ \dfrac{m^2}{\gamma}\left(\dfrac{1}{M_1^2} + \dfrac{\cos\alpha}{M_1}\right) \end{bmatrix}, \tag{A27}$$

where matrix $[\mathcal{A}]$ is given by Eq. (A19), with α replaced by α' in the last column. This solution is consistent with the one given by Moore[3] and checked by Mahesh *et al.*[16]

APPENDIX B: EXPRESSION FOR THE CIRCULATION

In this appendix an expression for the circulation in a half-plane is derived. We choose to evaluate the circulation in the lower half-plane which is positive for a hot spot. This can be computed by integrating the velocity given by Eqs. (9) and (10) over a segment ranging from $x = D$ to $-D$ and

a half-circle of radius D and letting D tend to ∞. Since $K(z)\approx -1/(2z^2)$ and $L(z)$ decays exponentially as $z\to\infty$ the integral over the half-circle vanishes, and

$$\frac{\Gamma}{U_2}=\frac{\epsilon}{\pi}\int_{+\infty}^{-\infty}dx\int_0^{\pi}\left[\Re(Z_{sv})K\left(\frac{x\cos\alpha}{c}\right)-\Im(Z_{sv})L\left(\frac{x\cos\alpha}{c}\right)\right]\sin\alpha^s J^s d\alpha^s. \tag{B1}$$

Since the integrals from $-\infty$ to ∞ of functions K and L are zero, the only term which will contribute to the circulation comes from the $\alpha^s=\pi/2$ slice. Writing $t=\cos\alpha^s/c$ and taking the α^s-dependent term out of the integral leads to

$$\frac{\Gamma}{aU_2}=-\frac{4\epsilon}{\pi}(Z_{sv}J^s(a/c))_{\pi/2}\int_0^{\infty}dx\int_0^1 K(xt)dt. \tag{B2}$$

For $\alpha^s=\pi/2$, Appendix A gives $Z_{sv}=1-m$, $J^s=1/m$, $c/a=1$, so the circulation can be written under the form

$$\frac{\Gamma}{aU_2}=\frac{2(m-1)}{m}f\epsilon, \tag{B3}$$

where f is a form factor which only depends upon the initial spot profile. For the Gaussian profile,

$$f=\frac{2}{\pi}\int_0^{\infty}dx\int_0^1 K(xt)dt=\sqrt{\pi}/2. \tag{B4}$$

For a constant spot, replacing function K by K^C in the above formula leads to $f=1$.

APPENDIX C: ASYMPTOTIC EXPRESSION FOR THE PRESSURE FIELD

In this appendix we develop an asymptotic expression of the pressure field given by Eq. (14), for large values of R/a, and away from the shock, so that we can neglect the nonpropagative field.

We first remark that around the point with coordinates (R,ϕ) the main contribution to the pressure field will come from the slice of angle $\alpha^p=\phi$, and from neighboring slices. This is illustrated in Fig. 6. Now, if R/a is large, the structure of these slices will not differ a lot from that corresponding to $\alpha^p=\phi$. So the pressure field is locally equivalent to the one generated by identical slices over an entire cylinder. So we write

$$\frac{p'}{P_2}\approx\frac{\epsilon}{\pi}(J^pZ_{sp})_{\phi}\int_{-\pi}^{\pi}K\left(\frac{\hat{r}^p-R}{b_{\phi}}\right)d\alpha^p, \tag{C1}$$

where the terms $(J^pZ_{sp})_{\phi}$ and b_{ϕ} represent the values of these functions for $\alpha^p=\phi$. Starting from this expression, we integrate both sides over the annular region between the circles of radii R and r. Dropping the factor $\epsilon/\pi(J^pZ_{sp})_{\phi}$ for sake of simplicity, the resulting expression is

$$2\pi\int_R^r\frac{p'}{P_2}(r')r'dr'\approx 2\pi\int_0^r 2\sqrt{r^2-x^2}K\left(\frac{x-R}{b_{\phi}}\right)dx-2\pi\int_0^R 2\sqrt{R^2-x^2}K\left(\frac{x-R}{b_{\phi}}\right)dx. \tag{C2}$$

The second term on the right-hand side is constant for fixed R and will disappear due to differentiation at a later stage, so we will drop it for now. The asymptotic behavior of the function $K(z)$ for $z\to\pm\infty$ is as z^{-2}, so we guess that the significant contribution of the first integral on the right-hand side is for $x\approx R$. We also wish to develop an asymptotic approximation valid in the vicinity of the cylindrical wave, i.e., $r\approx R$. So we approximate $\sqrt{r^2-x^2}=\sqrt{(r+x)(r-x)}\approx\sqrt{2R(r-x)}$ on the right-hand side, and $r'\approx R$ on the left-hand side. The resulting expression reads

$$R\int_R^r\frac{p'}{P_2}(r')dr'\approx\int_0^r 2\sqrt{2R(r-x)}K\left(\frac{x-R}{b_{\phi}}\right)dx. \tag{C3}$$

Then we set $x'=(r-x)/b_{\phi}$, so that

$$\int_R^r\frac{p'}{P_2}(r')dr'\approx-\sqrt{\frac{2}{R}}\int_0^{r/b_{\phi}}2\sqrt{b_{\phi}x'}K\left(\frac{r-R}{b_{\phi}}-x'\right)dx'. \tag{C4}$$

Remarking that the expression under the integral on the right-hand side term vanishes rapidly for $x'\to\infty$, we can replace the upper limit of the integral by ∞. After differentiation we are led to

$$\frac{p'}{P_2}(r)\approx-\sqrt{\frac{2}{R}}\int_0^{\infty}2\sqrt{\frac{x'}{b_{\phi}}}K'\left(\frac{r-R}{b_{\phi}}-x'\right)dx'. \tag{C5}$$

Then a last integration by parts leads to

$$\frac{p'}{P_2}\approx\sqrt{\frac{2b_{\phi}}{R}}\tilde{K}\left(\frac{r-R}{b_{\phi}}\right), \tag{C6}$$

where the function $\tilde{K}$ has the following expression:

$$\tilde{K}(z)=\int_0^{\infty}\frac{1}{\sqrt{z'}}K(z-z')dz'. \tag{C7}$$

An alternative integral definition of the function $\tilde{K}$ is given below, see Eq. (D19).

After reintroducing the angular factor, expression (25) is obtained.

APPENDIX D: GRASSO AND PIROZZOLI'S ACOUSTIC ANALOGY

In this appendix we reproduce the expression for the pressure field given by Grasso and Pirozzoli (GP) in Ref. 31 using an acoustic analogy of the problem, and compare this expression with our linear solution. In order to distinguish their work from ours, we will annotate all of the terms from GP's work with an overbar.

The main result from GP is their Eq. (17) which states

$$p'(\overline{\mathbf{x}},t)=\frac{1}{2^{3/2}\pi}\sqrt{C_2}(P_2-P_1)\times\left\{-\frac{\overline{H}\overline{r}^{-3/2}}{2}(1-M_2^2\sin^2\overline{\theta})^{-5/4}\cos\overline{\theta}+\frac{(d\overline{H}/d\tau)_{\tau=\tau}+\overline{r}^{-1/2}(1-M_2^2\sin^2\overline{\theta})^{-1/4}}{C_2(1-M_2^2)}\times[M_2-\cos\overline{\theta}(1-M_2^2\sin^2\overline{\theta})^{-1/2}]\right\}. \quad \text{(D1)}$$

The different terms entering this expression are defined as

$$\tau^+=t-\frac{\overline{r}}{C_2}\Phi^+, \quad \text{(D2)}$$

$$\Phi^+=\frac{\sqrt{1-M_2^2\sin^2\overline{\theta}}-M_2\cos\overline{\theta}}{1-M_2^2}, \quad \text{(D3)}$$

$$\overline{H}(\tau^+)=\int_{-\infty}^{r^+}\frac{\overline{K}(\tau)}{\sqrt{\tau^+-\tau}}d\tau, \quad \text{(D4)}$$

$$\overline{K}(\tau)=\int_{-\infty}^{+\infty}\left(\frac{1}{R}-1\right), \quad \text{(D5)}$$

and $R=\rho/\rho_1$ is the initial entropy distribution.

In order to compare with our linear solution we develop these expressions for the case of a Gaussian spot with radius a and amplitude $\epsilon\ll 1$, i.e.,

$$R=1-\epsilon\exp\left[\frac{-(x-U_1t)^2-y^2}{a^2}\right]. \quad \text{(D6)}$$

After a few manipulations, the different terms of GP's expression evaluate as follows:

$$\overline{K}(\tau)=\epsilon a\sqrt{\pi}\exp\left(-\frac{U_1^2\tau^2}{a^2}\right)=2\epsilon a K^I(U_1\tau/a), \quad \text{(D7)}$$

$$\overline{H}(\tau^+)=2\epsilon a^{3/2}U_1^{-1/2}\int_0^{\infty}\frac{K^I(U_1\tau/a-z')}{\sqrt{z'}}dz', \quad \text{(D8)}$$

$$(d\overline{H}/d\tau)_{\tau=\tau^+}=-2\epsilon a^{1/2}U_1^{1/2}\int_0^{\infty}\frac{L(U_1\tau/a-z')}{\sqrt{z'}}dz', \quad \text{(D9)}$$

where functions K^I and L are those defined in our Eqs. (16) and (12), and where the identity $dK^I(z)/dz=-L(z)$ has been used.

The expressions of GP are given in a frame centered on a point O_c located on the symmetry axis and on the shock front (see Fig. 22). Let us now consider a point M with coordinates $(\overline{r},\overline{\theta})$ in GP's frame and (r,ϕ) in our frame. We introduce the point M_0 with coordinates $(\overline{r_0},\overline{\theta})$ and (R,ϕ_0) in both frames, located on the line O_cM and on the circle of radius $R=C_2t$ centered on point O. At this point we have

$$\overline{r_0}\sin\overline{\theta}=R\sin\phi_0, \quad \text{(D10)}$$

$$\overline{r_0}\cos\overline{\theta}=R(\cos\phi_0+M_2). \quad \text{(D11)}$$

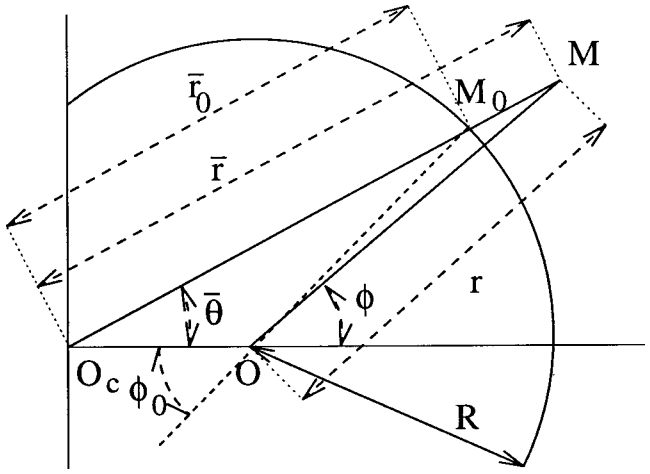

FIG. 22. Geometrical notations used in Grasso and Pirozzoli's analysis and in our analysis.

Using these geometrical identities, the following relations may be derived:

$$R/\overline{r_0}=\Phi^+, \quad \text{(D12)}$$

$$\frac{U_1\tau^+}{a}=\frac{mM_2\Phi^+(\overline{r_0}-\overline{r})}{a}. \quad \text{(D13)}$$

Using all these expressions, we rewrite expression (D1) in the limit of large time ($R/a\gg 1$). We neglect the first term proportional to $\overline{r}^{-3/2}$ and retain only the second term proportional to $\overline{r}^{-1/2}$. In the considered limit we also approximate $\overline{r}\approx\overline{r_0}$, $\phi\approx\phi_0$, and $\overline{r_0}-\overline{r}\approx(R-r)/\cos(\theta-\phi)$. This leads to

$$\frac{p'}{P_2}\approx\frac{-\epsilon\sqrt{2}}{\pi}(R/a)^{-1/2}\mathbf{F}_{\mathrm{GP}}(M_1;\phi)\tilde{L}\left(\frac{R-r}{b'}\right), \quad \text{(D14)}$$

where the terms $\mathbf{F}_{\mathrm{GP}}$, $\tilde{L}$, and b' are defined as

$$\mathbf{F}_{\mathrm{GP}}(M_1;\phi)=\frac{1}{2}\left(1-\frac{P_2}{P_1}\right)\sqrt{mM_2\Phi^+}\,\frac{(1-M_2^2\sin^2\overline{\theta})^{-1/4}}{1-M_2^2}\times\left[M_2-\frac{\cos\overline{\theta}}{\sqrt{1-M_2^2\sin^2\overline{\theta}}}\right], \quad \text{(D15)}$$

$$\tilde{L}(z)=\int_0^{\infty}\frac{L(z-z')}{\sqrt{z'}}dz', \quad \text{(D16)}$$

$$\frac{b'}{a}=\frac{\cos(\theta-\phi)}{mM_2\Phi^+}. \quad \text{(D17)}$$

[In Eq. (D15) $\overline{\theta}$ is defined implicitly as a function of ϕ using Eqs. (D3), (D10), and (D12) with $\phi=\phi_0$.]

We now compare the functions $\tilde{K}$ and $\tilde{L}$ appearing in Eqs. (25) and (D14). Introducing the integral definitions of functions K and L given by Eqs. (4) and (12) into Eqs. (27) and (D16), interverting the integrals over z' and k, and using the identity

$$\int_0^\infty \frac{\cos(k(z-z'))}{\sqrt{z'}}dz' = \int_0^\infty \frac{\sin(k(z+z'))}{\sqrt{z'}}dz' = \sqrt{\frac{\pi}{2k}}(\cos(kz)+\sin(kz)) \tag{D18}$$

leads to

$$\tilde{K}(z) = -\tilde{L}(-z) = \int_0^\infty \sqrt{\frac{k\pi}{8}}e^{-(k^2/4)}(\cos(kz)+\sin(kz))dk. \tag{D19}$$

We are finally led to expression (28).

[1] L. S. G. Kovasznay, "Turbulence in supersonic flow," J. Aero. Soc. **20**, 657 (1953).
[2] H. S. Ribner, "Convection of a pattern of vorticity through a shock wave," Technical Report No. 1164, NACA, 1953.
[3] F. K. Moore, "Unsteady oblique interaction of a shock wave with a plane disturbance," Technical Report No. 1165, NACA, 1954.
[4] C. Chang, "Interaction of a plane shock and oblique plane disturbances with special reference to entropy waves," J. Aero. Sci. **24**, 675 (1957).
[5] J. F. McKenzie and K. O. Westphal, "Interaction of linear waves with oblique shock waves," Phys. Fluids **11**, 2350 (1968).
[6] T. L. Jackson, A. K. Kalila, and M. Y. Hussaini, "Convection of a pattern of vorticity through a reacting shock wave," Phys. Fluids A **2**, 1260 (1990).
[7] P. W. Duck, D. G. Lasseigne, and M. Y. Hussaini, "The effect of three-dimensional freestream disturbances on the supersonic flow past a wedge," Phys. Fluids **9**, 456 (1997).
[8] H. S. Ribner, "Shock-turbulence interaction and the generation of noise," Technical Report No. 1233, NACA, 1954.
[9] T. A. Zang, M. Y. Hussaini, and D. M. Bushnell, "Numerical computations of turbulence amplification in shock–wave interactions," AIAA J. **22**, 13 (1984).
[10] S. Lee, S. K. Lele, and P. Moin, "Direct numerical simulations of isotropic turbulence interacting with a weak shock wave," J. Fluid Mech. **251**, 533 (1993).
[11] R. Friedrich and R. Hannappel, "On the interaction of wavelike disturbances with shocks: Two idealizations of the shock–turbulence interaction," Acta Mech. [Suppl.] **4**, 69 (1994).
[12] L. Jacquin, C. Cambon, and E. Blin, "Turbulence amplification by a shock wave and rapid distortion theory," Phys. Fluids **5**, 2539 (1993).
[13] H. S. Ribner, "The sound generated by interaction of a single vortex with a shock wave," Technical Report No. 61, University of Toronto, 1959.
[14] H. S. Ribner, "Cylindrical sound wave generated by the shock–vortex interaction," AIAA J. **23**, 1708 (1985).
[15] D. S. Dosanj and T. M. Weeks, "Interaction of a starting vortex as well as a vortex street with a travelling shock wave," AIAA J. **3**, 216 (1965).
[16] K. Mahesh, P. Moin, and S. K. Lele, "The interaction of a shock wave with a turbulent shear flow," Technical Report No. TF-69, Air Force Office of Scientific Research, 1996.
[17] K. Mahesh, S. K. Lele, and P. Moin, "The influence of entropy fluctuations on the interaction of turbulence with a shock wave," J. Fluid Mech. **324**, 353 (1997).
[18] F. E. Marble, G. J. Hendricks, and E. E. Zukoski, "Progress toward shock enhancement of supersonic combustion processes," Technical Report No. 87-1880, AIAA Paper, 1987.
[19] F. E. Marble, E. E. Zukoski, J. W. Jacobs, G. J. Hendricks, and I. A. Waitz, "Shock enhancement and control of hypersonic mixing and combustion," Technical Report No. 90-1981, AIAA Paper, 1990.
[20] R. P. Hamernik and D. S. Dosanjh, "Shock-induced dynamics of a low-density heated-fluid element," Phys. Fluids **15**, 1248 (1972).
[21] R. P. Hamernik and D. S. Dosanjh, "Generation of acoustic waves during the passage of a shock wave through a heated gaseous element," J. Acoust. Soc. Am. **53**, 921 (1973).
[22] G. Rudinger and L. M. Somers, "Behavior of small regions of different gases carried in accelerated gas flows," J. Fluid Mech. **7**, 161 (1960).
[23] G. H. Markstein, "Experimental studies of flame-front instability," in *Nonsteady Flame Propagations, AGARDograph No. 75* (Pergamon, Oxford, 1964), pp. 75–100.
[24] J.-F. Haas and B. Sturtevant, "Interaction of weak shock waves with cylindrical and spherical gas inhomogeneities," J. Fluid Mech. **181**, 41 (1987).
[25] J. W. Jacobs, "Shock-induced mixing of a light-gas cylinder," J. Fluid Mech. **234**, 629 (1992).
[26] J. M. Picone, E. S. Oran, J. P. Boris, and T. R. Young, "Theory of vorticity generation by shock wave and flame interactions," in *Dynamics of Shock Waves, Explosions, and Detonations*, edited by J. R. Bowen (AIAA, Washington, DC, 1985), pp. 429–448.
[27] J. M. Picone and J. P. Boris, "Vorticity generation by shock propagation through bubbles in a gas," J. Fluid Mech. **189**, 23 (1988).
[28] J. Yang, T. Kubota, and E. E. Zukoski, "Applications of shock-induced mixing to supersonic combustion," AIAA J. **31**, 854 (1993).
[29] J. Yang, T. Kubota, and E. E. Zukoski, "A model for characterisation of a vortex pair formed by shock passage over a light gas inhomogeneity," J. Fluid Mech. **258**, 217 (1994).
[30] M. Y. Hussaini and G. Erlebacher, "Interaction of an entropy spot with a shock," AIAA J. **37**, 346 (1999).
[31] F. Grasso and S. Pirozzoli, "Shock wave-thermal inhomogeneity interactions: Analysis and numerical simulations of sound generation," Phys. Fluids **12**, 205 (2000).
[32] M. Abramowitz and I. A. Stegun, *Handbook of Mathematical Functions* (Dover, New York, 1965).
[33] J. Sesterhenn, "A characteristic-type formulation of the Navier–Stokes equations for high order upwind schemes," Comput. Fluids **30**, 37 (2001).
[34] G. Moretti, "The λ-scheme," Comput. Fluids **7**, 191 (1979).
[35] N. A. Adams and K. Shariff, "A high-resolution hybrid compact-ENO scheme for shock–turbulence interaction problems," J. Comput. Phys. **127**, 27 (1996).
[36] J. H. Williamson, "Low-storage Runge–Kutta schemes," J. Comput. Phys. **35**, 48 (1980).
[37] G. Moretti, "Thoughts and afterthoughts about shock computations," Technical Report, PIBAL Report No. 72–73, Polytechnic Institute of Brooklyn, New York, December, 1972.
[38] G. Erlebacher, M. Y. Hussaini, and T. L. Jackson, "Nonlinear strong shock interactions: A shock-fitted approach," Theor. Comput. Fluid Dyn. **11**, 1 (1998).
[39] D. Fabre, "Interaction d'une onde de choc avec un champ porteur faiblement perturbé," Mémoire de DEA, Université Paris VI, 1998.
[40] D. Fabre, L. Jacquin, E. Garnier, and P. Sagaut, "Linear interaction analysis: The effect of a shock wave on a homogeneous perturbation field and on an entropy spot," in *Turbulence in High Speed Compressible Flows* (Poitiers, France, 1999), Euromech 403.